

**Numerical and Experimental Design of High Performance Heat Exchanger System for A  
Thermoelectric Power Generator for Implementation in Automobile Exhaust Gas Waste  
Heat Recovery**

Jaideep Pandit

Dissertation submitted to the faculty of the Virginia Polytechnic Institute and State University in  
partial fulfillment of the requirements for the degree of

Doctor of Philosophy

In

Mechanical Engineering

Srinath V. Ekkad Chair

Scott T. Huxtable Co-chair

Shashank Priya

Ranga Pitchumani

Khai D. T. Ngo

April 14, 2014

Blacksburg, VA

Keywords: Heat Transfer, Waste heat recovery, Thermoelectric Generators, Pin-fins, Jet  
Impingement

**Numerical and Experimental Design of High Performance Heat Exchanger System for A Thermoelectric Power Generator for Implementation in Automobile Exhaust Gas Waste Heat Recovery**

Jaideep Pandit

**ABSTRACT**

The effects of greenhouse gases has seen a significant rise in recent years due to the use of fossil fuels like gasoline and diesel. Conversion of the energy stored in these fossil fuels to mechanical work is an extremely inefficient process which results in a high amount of energy rejected in the form of waste heat. Thermoelectric materials are able to harness this waste heat energy and convert it to electrical power.

Thermoelectric devices work on the principle of the Seebeck effect, which states that if two junctions of dissimilar materials are at different temperatures, an electrical potential is developed across them. Even though these devices have small efficiencies, they are still an extremely effective way of converting low grade waste heat to usable electrical power. These devices have the added advantage of having no moving parts (solid state) which contributes to a long life of the device without needing much maintenance. The performance of thermoelectric generators is dependent on a non-dimensional figure of merit,  $ZT$ . Extensive research, both past and ongoing, is focused on improving the thermoelectric generator's (TEG's) performance by improving this

figure of merit,  $ZT$ , by way of controlling the material properties. This research is usually incremental and the high performance materials developed can be cost prohibitive.

The focus of this study has been to improve the performance of thermoelectric generator by way of improving the heat transfer from the exhaust gases to the TEG and also the heat transfer from TEG to the coolant. Apart from the figure of merit  $ZT$ , the performance of the TEG is also a function of the temperature difference across it, By improving the heat transfer between the TEG and the working fluid, a higher temperature gradient can be achieved across it, resulting in higher heat flux and improved efficiency from the system. This area has been largely neglected as a source of improvement in past research and has immense potential to be a low cost performance enhancer in such systems. Improvements made through this avenue, also have the advantage of being applicable regardless of the material in the system. Thus these high performance heat exchangers can be coupled with high performance materials to supplement the gains made by improved figure of merits.

The heat exchanger designs developed and studied in this work have taken into account several considerations, like pressure drop, varying engine speeds, location of the system along the fuel path, system stability etc. A comprehensive treatment is presented here which includes 3D conjugate heat transfer modeling with RANS based turbulence models on such a system. Various heat transfer enhancement features are implemented in the system and studied numerically as well as experimentally. The entire system is also studied experimentally in a scaled down setup which provided data for validation of numerical studies. With the help of measured and calculated data like temperature,  $ZT$  etc, predictions are also presented about key metrics of system performance.

Dedicated to my parents, Sushama and Madhav Pandit whose love, support and encouragement has made this possible.

## Acknowledgements

I would like to acknowledge several people without whom this work would not have been possible. Foremost, I would like to express my deepest gratitude to Dr. Srinath Ekkad and Dr. Scott Huxtable, my advisors and mentors, who have provided countless hours of expert guidance and advice. The responsibility and trust they have put in me throughout my graduate career has been immensely important in my development as a researcher.

My advising committee members, Dr. Priya, Dr. Pitchumani and Dr. Ngo have been instrumental in providing valuable insight and guiding this research, and for that, I'm very grateful. I would also like to acknowledge all the teachers I have had throughout the past 20 years. Their extraordinary efforts have been critical in inspiring and driving me towards getting an advanced degree. I would also like to acknowledge the funding agency that supported this project. This material is based upon work supported by the National Science Foundation and Department of Energy through the NSF/DOE Joint Thermoelectric Partnership, Grant No. CBET-1048708.

I could not have achieved half of what I have without the help of colleagues and friends. I have had the good fortune of working with amazing people over the past few years, who have provided support, guidance, criticism and insight as and when I needed it. For this I would like to thank all the former and current members of the HEFT lab and other colleagues at Virginia Tech, Dr. Parida, Dr. Abraham, Dr. Panchal, Dr. Narzary, Dr. Lamont, Dr. Leblanc, Dr. Roy, Dr. Delimont, Dr. Song, Preston, Sridharan, Megan, Jayati, Dorian, David, Hunter, Sakshi, Ryan, Shreyas, Willis, Andrew, Sandeep, Kartikeya, Kris, Li. I would especially like to thank Megan

and Jayati, who have spent countless hours helping me work on various aspects of this project. I would also like to thank Diana Israel who is an unbelievable administrator and a fantastic person.

The friends I have had, cannot be thanked enough for their support throughout my academic career. Utkarsh, Niket, Ankit, Anand, Bharat, Gaurav, Karan, Sumeet, Gaurang, Sneha, Priyanka, Shalini, Deepika, Paridhi, Shikha ,Asmita, Gaurav, Saloni, Keyur, Varun, Balaji, Sudeeksha, Kartik- all of you have my deepest gratitude, for in one way or another, you have all shaped me.

Anushree, you have been my support system over the past several years and for that I cannot thank you enough. Finally and most importantly, I would like to acknowledge my family, without whom I could have achieved nothing. Didi, Mamma, Baba, I don't have the words to express how much I owe you. You are my oasis.

## Table of Contents

ABSTRACT.....	ii
Acknowledgements.....	v
List of figures.....	ix
List of Tables.....	xii
Preface.....	1
INTRODUCTION.....	2
Chapter 1: Baseline Design of Heat Exchanger.....	7
Numerical Method.....	8
Geometry and Boundary Conditions –Baseline Case.....	8
Results- Baseline Case.....	9
Hot Side Temperatures.....	10
Cold Side Temperatures.....	10
Other Important Results.....	11
Chapter 2: Coolant Side Heat Transfer Enhancement.....	16
Guided Coolant.....	17
Impinging Jets in Coolant Domain.....	20
Comparison.....	21
Conclusion.....	24
Chapter 3: Exhaust Gas Side Heat Transfer Enhancement.....	25
Experimental Setup.....	27
Methodology.....	31
Wall Temperature Calculation.....	32
Uncertainty.....	37
Results & Discussion.....	37
Conclusions.....	47
Chapter 4: Experimental Investigation of Heat Transfer in Thermoelectric Generator for Automotive Exhaust Waste Energy Harvesting.....	49

Experimental Setup .....	50
Test Section .....	52
Test Matrix .....	56
Methodology .....	57
Results & Discussion .....	60
Conclusion.....	74
Chapter 5: An Analysis of effect of contact conductance on system performance efficiency and power generation.....	75
Theory .....	76
Methodology .....	80
Geometry and Boundary Conditions.....	80
Results & Discussion .....	81
Conclusions .....	85
CONCLUSIONS.....	86
NOMENCLATURE .....	88
REFERENCES .....	90

## List of figures

<b>Figure 1:</b> Generating efficiency as a function of temperature and thermocouple material figure-of merit. Adapted from Rowe et al [2].....	3
<b>Figure 2:</b> Schematic for installation of TEG .....	6
<b>Figure 3:</b> Geometry for the Baseline Case .....	9
<b>Figure 4:</b> Temperature contour for the hot side - Baseline Geometry.....	11
<b>Figure 5:</b> Area averaged temperature plot for each module on the hot side - Baseline Geometry .....	12
<b>Figure 6:</b> Temperature contour for the cold side - Baseline Geometry.....	13
<b>Figure 7:</b> Area averaged temperature plot for each module on the cold side - Baseline Geometry.....	13
<b>Figure 8:</b> Streamlines showing flow of coolant-Baseline Geometry .....	14
<b>Figure 9:</b> Area averaged temperature plot for each module on the cold side - Baseline Geometry.....	15
<b>Figure 10:</b> Two views to illustrate the geometry of the guided coolant domain.....	18
<b>Figure 11:</b> Streamlines showing flow of coolant-Guided Coolant Geometry.....	18
<b>Figure 12:</b> Plot for temperature difference (area averaged) across each module- Guided Coolant Geometry .....	19
<b>Figure 13:</b> Temperature contours on the hot and cold side of the Thermoelectric Modules for the guided coolant geometry.....	19
<b>Figure 14:</b> Two views to illustrate the location of impinging jets in the coolant domain.....	20
<b>Figure 15:</b> Streamlines showing flow of coolant-Impinging Coolant Geometry.....	21
<b>Figure 16:</b> Plot for temperature difference (area averaged) across each module- Impinging Coolant Geometry .....	22
<b>Figure 17:</b> Comparison of quantities of interest for the three cases.....	23
<b>Figure 18:</b> Schematic of the test facility. ....	28
<b>Figure 19:</b> Experimental test section.....	29
<b>Figure 20:</b> Top view of the pin fin configuration.....	30
<b>Figure 21:</b> Front view of the test section.....	30
<b>Figure 22:</b> Typical calibration curve for the Transient Liquid Crystal (TLC) measurements.. ..	34

<b>Figure 23:</b> Heat transfer coefficient as measured with the transient liquid crystal technique.....	36
<b>Figure 24:</b> Heat transfer coefficients for various pin fin shapes as measured by the transient liquid crystal technique at a Reynolds number of 5,000.....	38
<b>Figure 25:</b> Spanwise area averaged normalized Nusselt numbers for Reynolds numbers of (a) 5,000, and (b) 10,000.....	40
<b>Figure 26:</b> Normalized Nusselt number for the different pin fin shapes at Reynolds numbers of 5,000 and 10,000. ....	42
<b>Figure 27:</b> Heat transfer coefficient distribution with varying Reynolds number and $h/H$ ratios for diamond shaped pin fins. ....	43
<b>Figure 28:</b> Normalized Area Averaged Nusselt number for different pin fin heights as a function of Reynolds number. ....	44
<b>Figure 29:</b> Spanwise area averaged normalized Nusselt numbers for different Reynolds numbers with varying $h/H$ ratios. . ....	46
<b>Figure 30:</b> Spanwise line averaged normalized Nusselt numbers for Reynolds numbers between 5,000 and 20,000 and $h/H$ ratios of 25 % and 50 %.....	47
<b>Figure 31:</b> Layout of the baseline heat exchanger.....	51
<b>Figure 32:</b> Front view of the layout of the heat exchanger.. ....	51
<b>Figure 33:</b> Cold side baseline geometry test section piece.....	53
<b>Figure 34:</b> Hot side test section piece.. ....	53
<b>Figure 35:</b> Cold side baseline geometry.....	54
<b>Figure 36:</b> Cold side impingement jet geometry.....	55
<b>Figure 37:</b> Exhaust side pin-fin geometry.....	55
<b>Figure 38:</b> Schematic of the hot loop. ....	58
<b>Figure 39:</b> Schematic of the cold loop. ....	58
<b>Figure 40:</b> Figure illustrating location of thermocouples for temperature measurement. ....	59
<b>Figure 41:</b> Numbering of thermocouples on the TEG.....	59
<b>Figure 42:</b> Variation in hotside temperature with varying engine RPM. Three different hot side inlet temperatures are examined at a fixed coolant mass flow rate capacity of 60%.....	62

<b>Figure 43:</b> Variation in hotside temperature with varying engine RPM. Three different hot side inlet temperatures are examined at a fixed coolant mass flow rate capacity of 100%.....	64
<b>Figure 44:</b> Variation in cold side temperature with varying engine RPM. An exhaust gas inlet temperature of 400 ° C is examined at coolant mass flow rate capacities of 60% and 100%.....	66
<b>Figure 45:</b> Variation in $\Delta T$ with varying engine RPM. Three different hot side inlet temperatures are examined at a fixed coolant mass flow rate capacity of 60%. .....	69
<b>Figure 46:</b> Variation in $\Delta T$ with varying engine RPM. Three different hot side inlet temperatures are examined at a fixed coolant mass flow rate capacity of 100%. .....	70
<b>Figure 47:</b> Increase in efficiency of the TEG with varying geometry combinations. (Exhaust gas inlet@ 400°C, 1900 RPM, 100% coolant MFR capacity).....	73
<b>Figure 48:</b> Effective increase in ZT required to achieve same gain in efficiency for various cases. ....	73
<b>Figure 49:</b> Typical thermal circuit in a thermoelectric energy harvesting device.....	77
<b>Figure 50:</b> Thermoelectric hot side average temperature variation with thermal contact resistance .....	82
<b>Figure 51:</b> Thermoelectric cold side average temperature variation with thermal contact resistance .....	83
<b>Figure 52:</b> Average temperature difference between hot and cold side vs. thermal contact resistance .....	83
<b>Figure 53:</b> Projected thermoelectric efficiency vs. thermal contact resistance .....	84

## List of Tables

<b>Table 1:</b> Thermal Properties of $\text{Bi}_2\text{Te}_3$ .....	8
<b>Table 2:</b> Test matrix for the experiments. ....	56
<b>Table 3:</b> Temperature data for Baseline-Baseline case .....	71
<b>Table 4:</b> Temperature data for Baseline-Impingement case.....	71
<b>Table 5:</b> Temperature data for Pin-fins-Baseline case .....	72
<b>Table 6:</b> Temperature data for Pin-fins-Impingement case.....	72

## **Preface**

This dissertation portrays the design, development, testing and analysis of a heat exchanger system for waste heat recovery system for automotive exhaust gases, in a systematic manner. The author was responsible for development of this system from the beginning of this NSF/DOE Joint Thermoelectric Partnership which aims at developing a thermoelectric solution to recover the wasted heat in exhaust gases of an automobile and reduce the dependence on the alternator by acting as an auxiliary power system.

The dissertation consists of five chapters, which have are based on manuscripts that have either been submitted/accepted or are in preparation for submission to archival journals. Each chapter highlights the evolution of the heat exchanger design and the improvement in performance that is achieved by improvements in design. The first two chapters detail the development of the first heat exchanger for such a system and explores the improvements that can be made to the coolant loop for contribution to the efficiency. The third chapter explores pin-fins as a heat transfer augmentation technique on the hot side (exhaust side) of the system. This study is done experimentally with the use of a high resolution temperature mapping technique (transient liquid crystal thermography) The fourth chapter experimentally studies the entire system with all heat transfer augmentation techniques implemented and provides data for validation of the numerical studies performed in chapter 1. Finally, the last chapter investigates the effects of thermal contact conductance on the performance of the system as a whole.

## INTRODUCTION

Thermoelectric power generators are being investigated aggressively as a viable source of waste heat recovery from automobile exhaust gases. The principle involved is the Seebeck effect which allows for the conversion of a temperature gradient into electrical power. Since there is already a high temperature source available in the form of exhaust gases, thermoelectric devices may be used to harness this temperature difference between the hot gas and the atmosphere or coolant. Waste heat energy recovery using thermoelectric elements may be used in any such application where a hot source and a cold sink are available. This method is more viable than ever now due to the greatly improved performance of newer thermoelectric materials whose conversion efficiencies have increased more than three fold since the 1980s [1]

The efficiency of a TEG (Thermoelectric Generator) may be thought of as the ratio of the power output to the heat input at the hot junction. This ratio is governed by the laws of thermodynamics and cannot thus exceed the Carnot efficiency. It follows that the greater the difference between the hot and cold side temperatures, the greater the efficiency of the TEG. The performance parameter of thermoelectric materials is  $Z$ , where,

$$Z = \frac{\alpha^2 \sigma}{\lambda} \quad \text{Equation 1}$$

where  $\alpha^2 \sigma$  is called the electrical power factor,  $\alpha$  is the Seebeck coefficient,  $\sigma$  is electrical conductivity and  $\lambda$  is the total thermal conductivity. The more useful and popular figure of merit is the dimensionless form  $ZT$  ( $T$ , absolute temperature).

Efficiency of the TEG is given by,

$$\eta = \frac{\Delta T}{T_h} \frac{\sqrt{1 + ZT} - 1}{\sqrt{1 + ZT} + T_c/T_h} \quad \text{Equation 2}$$

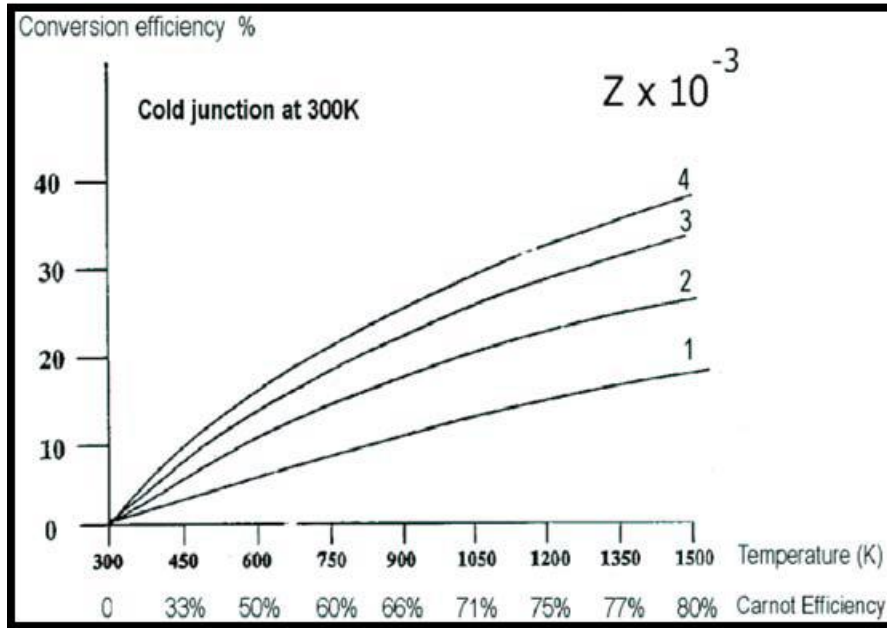


**Figure 1::** Generating efficiency as a function of temperature and thermocouple material figure-of merit.

Adapted from Rowe et al [2].

The efficiency of typical IC engines is 37-50% [3]. Of the fuels total energy, approximately 40% is lost to the exhaust gases [4]. A significant portion of the engine power is utilized in running the alternator for providing electrical power for features such as air conditioning, headlights etc. Approximately 10% of engine power may be made available by harnessing about 6% of the energy in exhaust gases and using it towards work ordinarily done by the alternator [5]. The typical efficiencies of thermoelectric materials are extremely low (< 10 %). This efficiency depends, among other things, on the temperature difference available to the device. The

efficiency of these generators may increase by as much as 0.04 per degree of the difference [6]. Therefore, it is important to develop an efficient heat exchanger for use with the generator in order to realize the full potential of the available power. Along with being thermally capable and efficient, the heat exchanger must also be dynamically stable and must allow for expansion of the TEG materials due to the high temperatures involved.

There are, however, several challenges in designing the heat exchanger. Since the space available to install this heat exchanger is limited, it is difficult to increase the surface areas of the heat exchanger. In order to compensate for this limitation, more heat transfer enhancement features have to be added. This leads to an increased pressure drop which in turn causes increased load on the alternator to supply the increased power requirement of the coolant pump. The cost of manufacture and installation of the system is also a major factor. Therefore it is important to determine the trade-off between a larger temperature difference across the TEG, the cost to install and the gain in efficiency for the vehicle. Another factor which might need consideration, though to a lesser extent, is the drop in efficiency due to the added weight.

Apart from the considerations above, another important decision point is the location of the TEG. It would be beneficial from a heat exchanger point of view if the hot side were installed immediately after the exhaust manifold, as this is where the exhaust gases will be the hottest. However, this would result in reduced temperatures at the catalytic converter, negatively affecting its performance. It is for this reason that manufacturers are reluctant to put any energy scavenging the catalytic converter.

Several studies have focused on creating experimental TEG exhaust systems and improving the heat transfer to the TEG. For example, work done by Zorbas et al. [7] and Chen et al. [8] focused

on experimental investigation of the heat transfer to the TEG, but tended to use lower temperatures in the hot air flow. Other work done by Wojciechowski et al [5] and Vazquez et al.[3] use actual internal combustion engines as the means of heating and moving the gas for the hot side loop. Vazquez et al. additionally used the coolant system in the engine as the coolant loop for the cold side of the test section. These studies conclude that the heat available to the system depends greatly on not only the speed but also the torque produced. Vazquez found that the thermoelectric generator worked best at 65mph going uphill at a slight gradient (2-3%) for their heat exchanger design. This has been attributed to optimum conditions of mass flow rate and temperature of the exhaust gases produced at the observed speed and torque from the engine.

Several different heat exchanger designs have been tested for effectiveness. Crane and Lagrandeur [9] changed design geometries from a flat plate design to a cylindrical hot side that included a bypass exhaust system. They reported an improvement of 1-7% in fuel economy based on the bench test data. Serksnis [10] also used a cylindrical design. Bass et al [11] used a design that was similar to Serksnis' design, though it is more hexagonal than cylindrical. The coolant in this case is applied by a cold plate, held by adjusting screws and springs to keep tension on the TEG. Many studies choose to use a flat plate design, such as those done by Birkholz et al. [12], Ikoma et al., [13], Espinosa et al. [14], and Saqr et al. [1]. Ikoma et al. used two aluminum water cooled jackets to cool the cold side of the TEG, and Saqr et al. used a cold plate based on a radiator design, using both coolant and the air moving past the vehicle to cool the TEG.

Saqr et al. give a comprehensive background on earlier, less efficient, thermoelectric generation designs for automobiles.

Typical research in this field is related to development of new thermoelectric elements. This has however been a fairly difficult area of research. Here, the focus of research is on increasing the temperature difference available to the TEG in order to improve efficiency and power production. Based on the considerations listed so far, it was decided to place the TEG after the catalytic converter. This design uses a bypass in the exhaust pipe (Figure 2) in order to increase the surface area without modifications to the existing design. This could also serve the purpose of regulating the flow into the TEG based on optimum conditions for power generation.

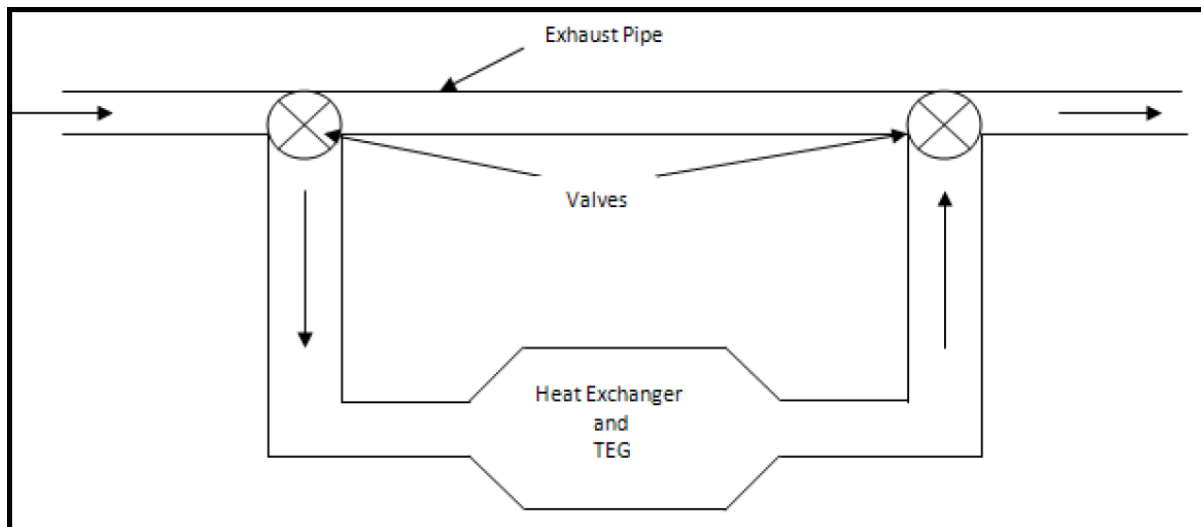


**Figure 2: Schematic for installation of TEG**

# **Chapter 1: Baseline Design of Heat Exchanger**

## BASELINE DESIGN

Based on the considerations outlined in the previous chapter, a design was developed that could be implemented in an automobile without major modifications to it. This chapter outlines the design of this heat exchanger and the methodology followed for characterization of this baseline system. Results from this analysis are also shown.

### Numerical Method

The designs in this study were modeled using commercially available software, ANSYS CFX. The  $k-\omega$  model was used for turbulence. The thermoelectric material considered was Bismuth Telluride ( $\text{Bi}_2\text{Te}_3$ ), the thermal properties for which can be seen in Table 1.[15]

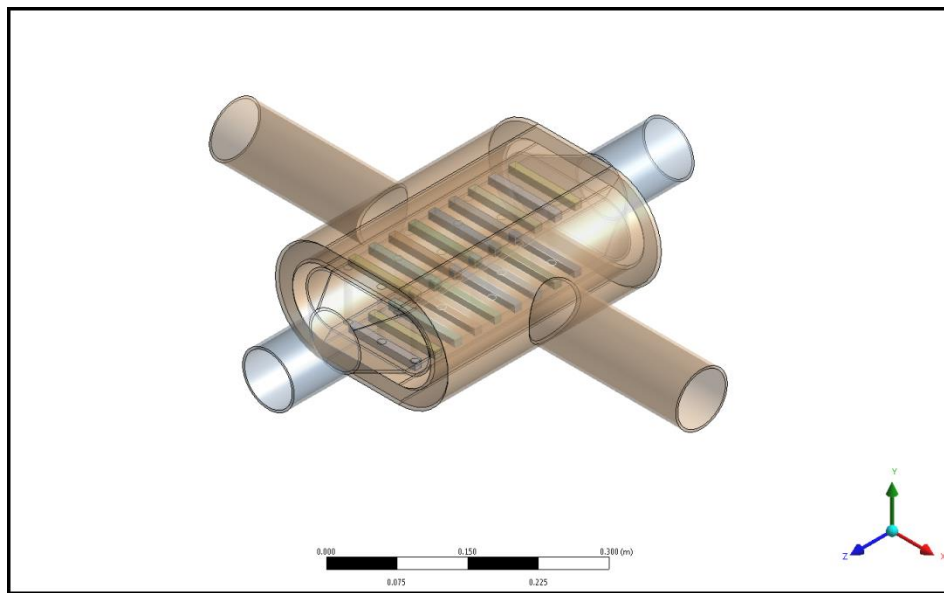
Quantity	N Type	P Type
Thermal Diffusivity	0.011	0.011
Density ( $\text{g}/\text{cm}^3$ )	7.683	6.630
$C_p$	0.159	0.186
Thermal Conductivity ( $\text{W}/\text{mK}$ )	1.344	1.356

Table 1: Thermal Properties of  $\text{Bi}_2\text{Te}_3$

### Geometry and Boundary Conditions –Baseline Case

The geometry (Figure 3) consists of a pipe containing the exhaust gases expanding into a flattened-oval section in order to slow them down and increase surface area. Vertical pipes pass through the channel in order to enhance conduction, create turbulence and promote mixing in the exhaust gases. The representative TEG geometries (material- $\text{Bi}_2\text{Te}_3$ ) are attached to the flat surfaces of the oval sections. A channel containing the coolant flowing in a direction perpendicular to the exhaust gas is wrapped around this.

The exhaust gas pipe is considered adiabatic in order to get its temperature to the exhaust gas temperature as might be expected. Similar reasoning applies for the coolant pipe. The exhaust gas inlet velocity is taken to be 20 m/s based on a 2.4 l, v6 engine at 3000 RPM and the cross section of the pipe. The hot side gas temperature at inlet to the heat exchanger is assumed to be 400 °C. For the coolant, the maximum mass flow rate is assumed to be 10 l/min and temperature is 100 °C [16].



**Figure 3: Geometry for the Baseline Case**

### **Results- Baseline Case**

In this section, relevant results from the baseline case are presented. An estimate of the power generated from such a case is also made. These results will enhance the understanding of reasoning behind modifications made to the geometry in the following sections. The two most

important quantities from the point of view of a thermoelectric generator are the temperatures on the hot and cold side. Also, the pressure drop in the two fluid domains needs to be assessed.

### **Hot Side Temperatures**

Figure 4 shows a contour plot for the temperatures on the hot side of the thermoelectric materials. The plot is oriented such that the exhaust gas comes in from the top. This is where the temperatures are the highest. The middle section drops in temperature as the coolant flows over that section. The temperature range at the hot side is approximately from 291-332 °C. The Figure 5 shows area averaged temperature for each thermoelectric module representative. Numbering of the modules starts from the top.

The plot in Figure 5 also conveys the same information as Figure 4. However, this data is useful in estimating projected power generation from the modules based on temperature gradients across them.

### **Cold Side Temperatures**

A similar analysis of the cold side temperatures is performed in Figure 6 and Figure 7. As in the case of hot side, the temperature peaks at the top of the plot. The coldest zones are in the middle where the majority of the coolant flows over. The average temperatures from Figure 7 highlight the same trends.

### Other Important Results

In order to determine what the reason behind a non-uniform drop in temperature on the cold and hot sides, the streamlines in the cold flow were examined. They are presented in Figure 8. The streamlines clearly show that the bulk of the coolant flows over the middle section of the assembly. Since there is not much active flow at the ends, the temperatures there are generally higher. One of the designs explored in this study aims to correct this situation by setting up flow guide in the coolant domain.

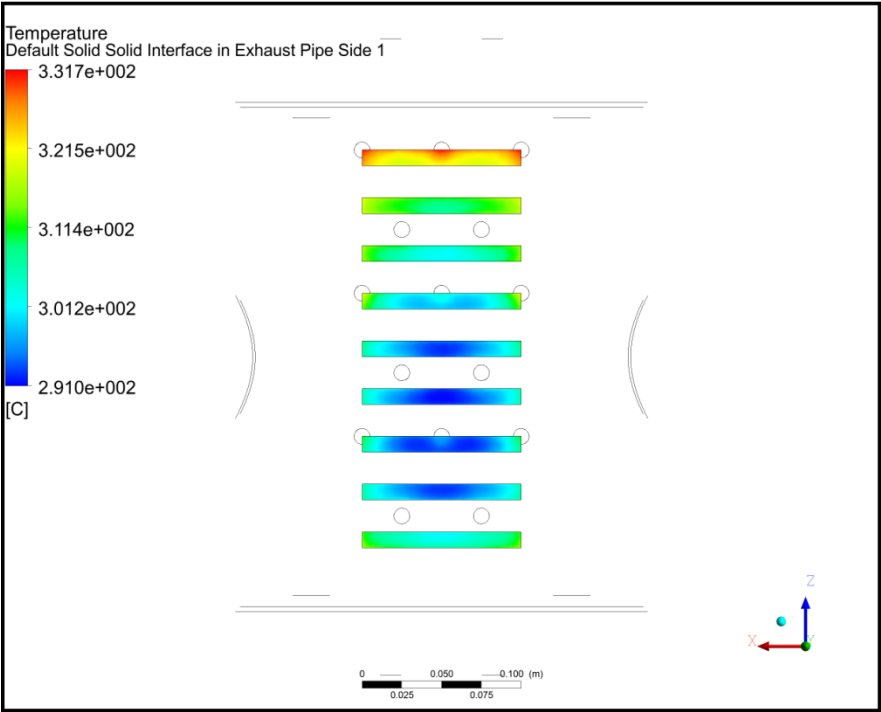
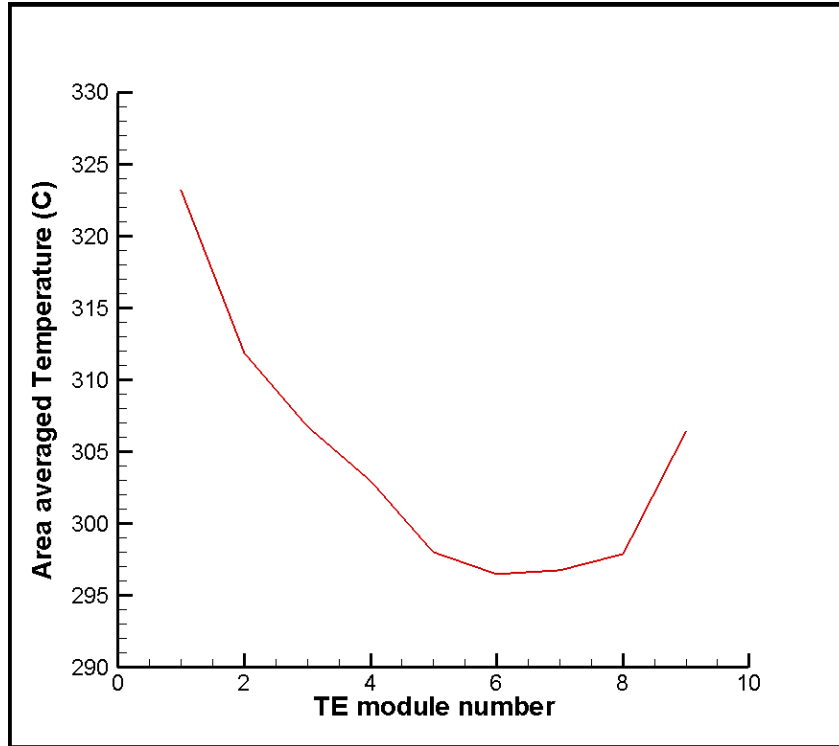


Figure 4: Temperature contour for the hot side - Baseline Geometry



**Figure 5: Area averaged temperature plot for each module on the hot side - Baseline Geometry**

Another quantity of interest is the overall pressure drop. With the baseline case, the pressure drop over the exhaust gas domain is approximately 77 Pa and it is 1.55 Pa in the coolant domain.

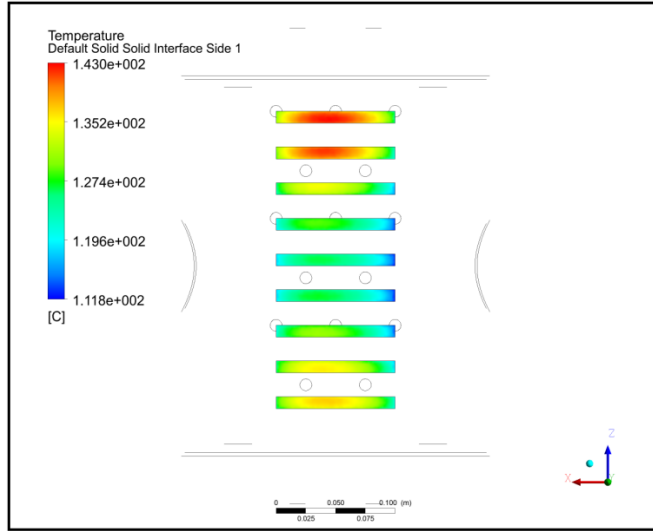


Figure 6: Temperature contour for the cold side - Baseline Geometry

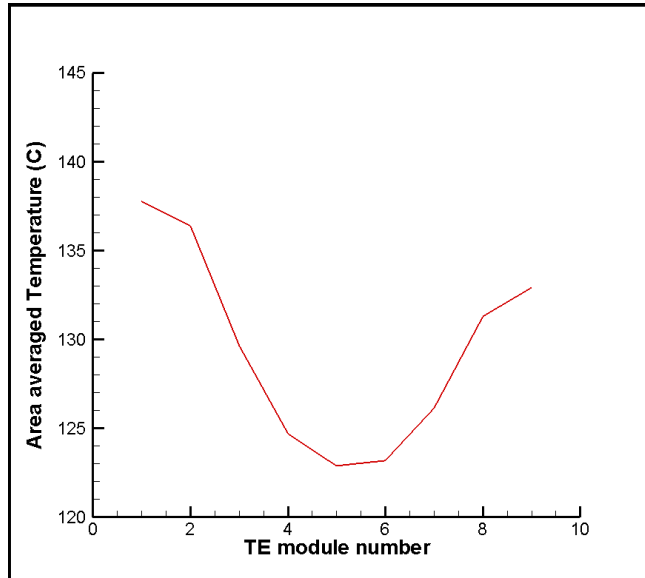
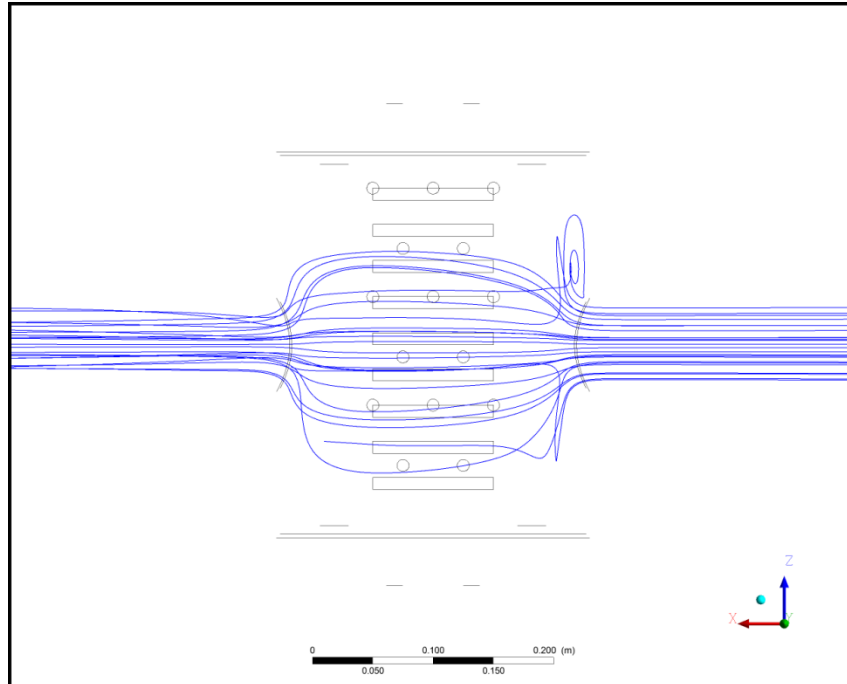


Figure 7: Area averaged temperature plot for each module on the cold side - Baseline Geometry



**Figure 8: Streamlines showing flow of coolant-Baseline Geometry**

A key point of interest is the temperature difference across each thermoelectric module. This is shown in Figure 9. From the plot, the difference between the temperatures is close to 170 °C. The average value for the difference is 175 °C.

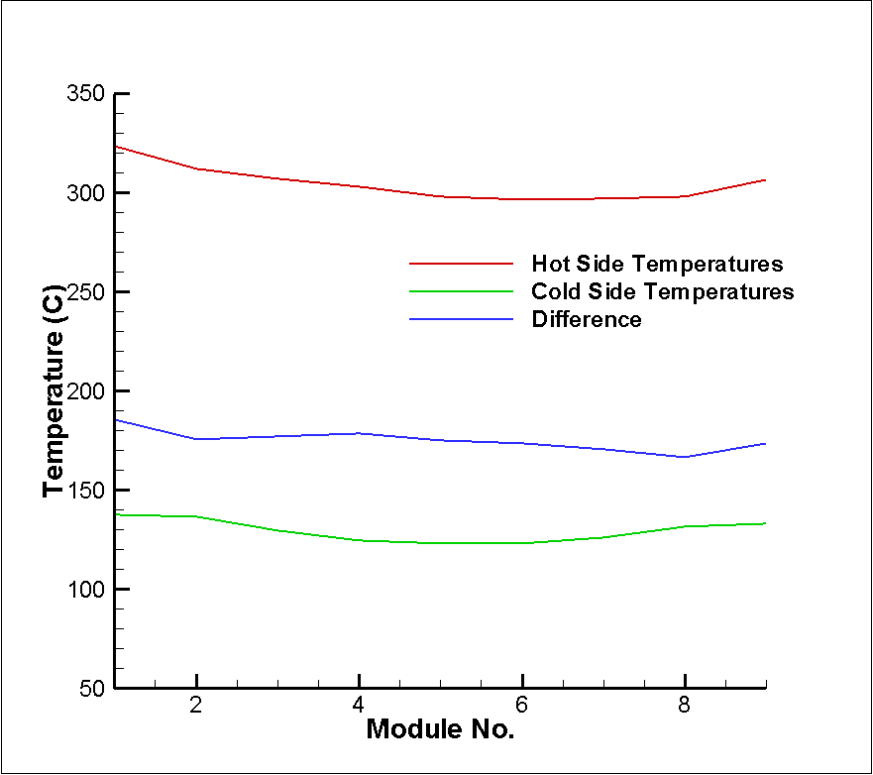


Figure 9: Area averaged temperature plot for each module on the cold side - Baseline Geometry

## **Chapter 2: Coolant Side Heat Transfer Enhancement**

## **COOLANT SIDE HEAT TRANSFER ENHANCEMENT**

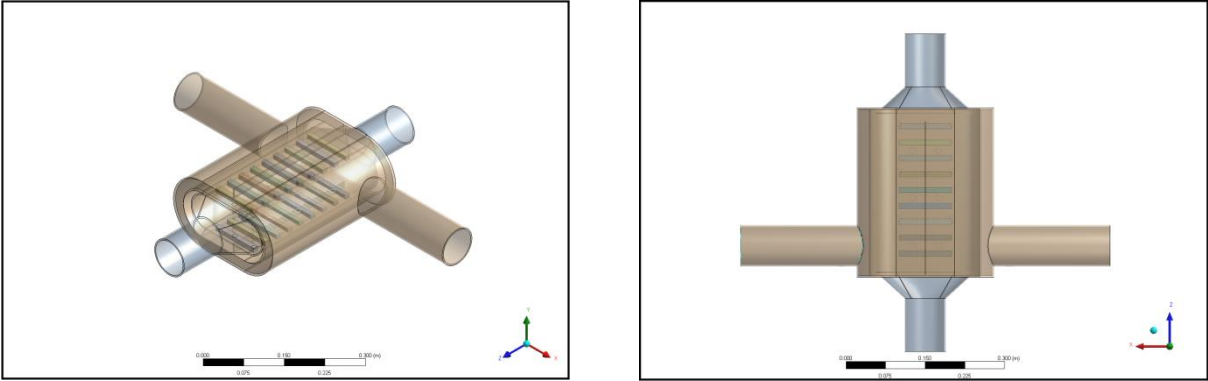
Building on the baseline case, two more geometries were explored. These geometries make modifications to the coolant loop in the system so as to enhance the heat transfer coefficient on the cold side of the thermoelectric modules. This helps achieve lower temperatures at the cold side and a larger temperature difference. As discussed earlier, each additional degree of temperature difference can increase the efficiency of the power output by 0.04% points [6].

### **Guided Coolant**

This geometry of the coolant domain seeks to encourage a more uniform flow over the cold side of the modules by adding a flow guide to the domain. This was motivated by the streamlines in Figure 8. The geometry is shown in Figure 10. The coolant enters from towards the end instead of the middle of the section. The flow is guided by a partition running across the domain. The flow pattern is illustrated in Figure 11.

The coolant flows in from the right side exits on the left side. The partition in the flow domain forces it to flow over the entire domain instead of having the bulk of the flow at the center of the section. This configuration makes the temperatures more uniform on both sides. A plot showing temperatures at and difference across the hot and cold side for the guided coolant geometry is shown in Figure 12. Not only is the difference more uniform but it is also higher than in the case of the baseline geometry. The average value of the area averaged temperature difference is  $184.006^{\circ}\text{C}$ . The corresponding contour plots for the temperature at the hot and cold side are

shown in Figure 13. The pressure drop in the exhaust section was found to be the same as the baseline case and increases to 38 Pa in the coolant domain.



(a) Isometric View

(b) Top View

**Figure 10: Two views to illustrate the geometry of the guided coolant domain**

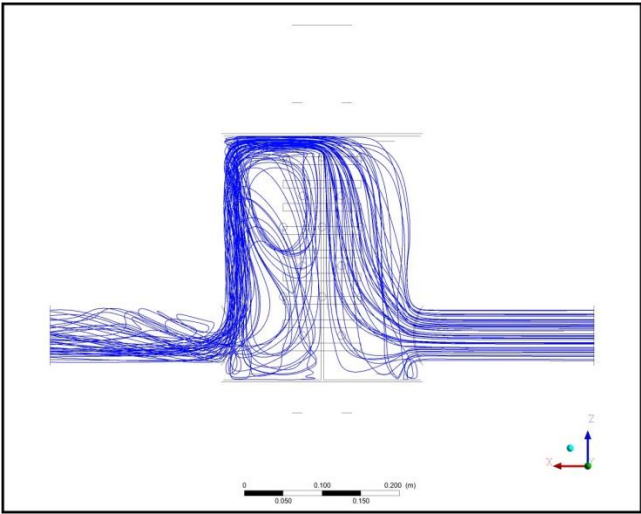


**Figure 11: Streamlines showing flow of coolant-Guided Coolant Geometry**

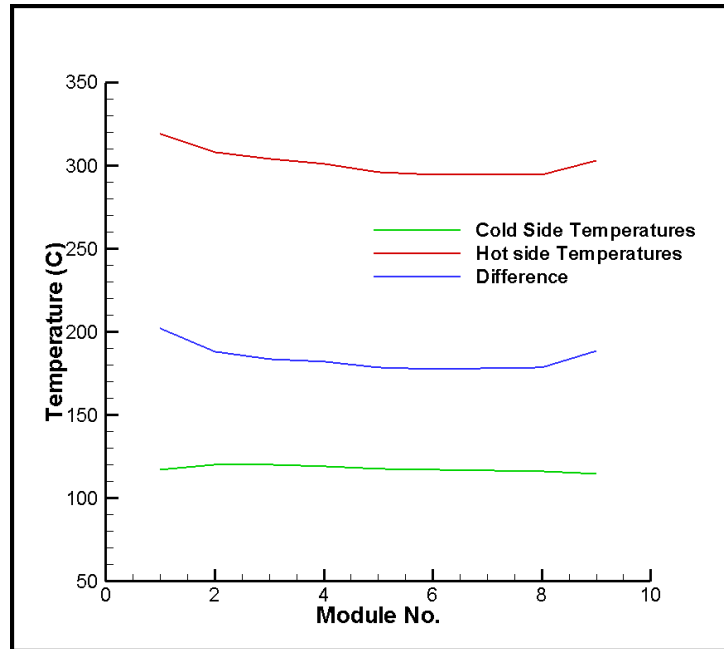
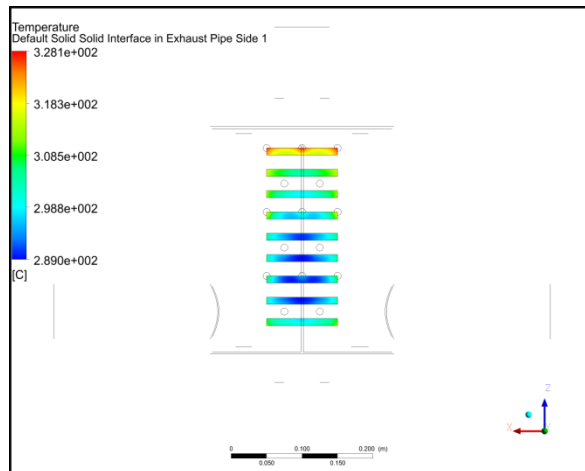
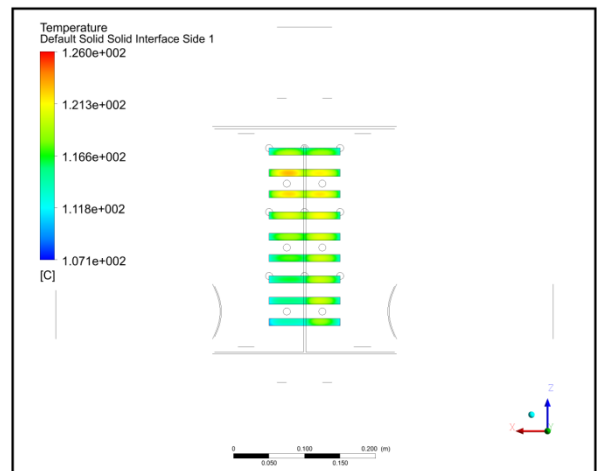


Figure 12: Plot for temperature difference (area averaged) across each module- Guided Coolant Geometry



(a) Hot Side

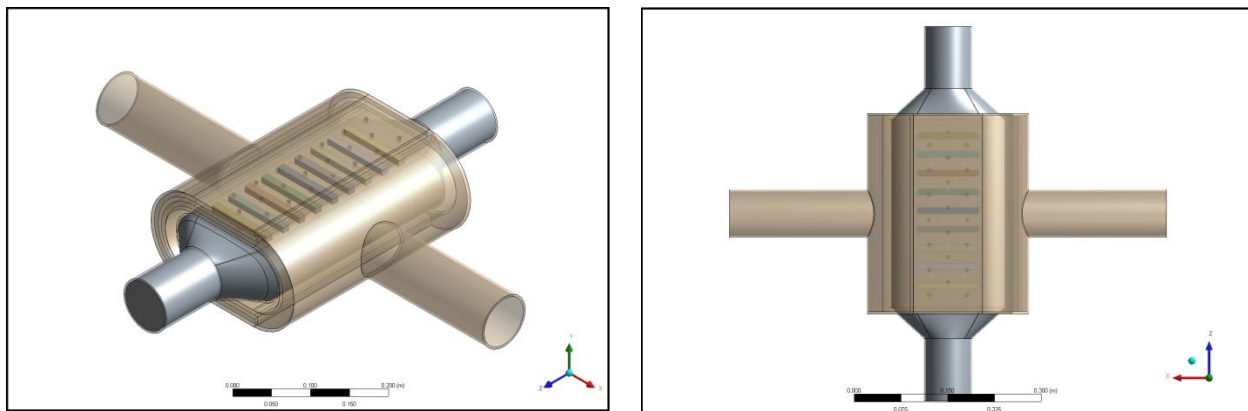


(b) Cold Side

Figure 13: Temperature contours on the hot and cold side of the Thermoelectric Modules for the guided coolant geometry

## Impinging Jets in Coolant Domain

The next geometry studied included impinging jets in the coolant domain. These jets impinge on the section of the pipe in contact with the cold side of the thermoelectric modules. Figure 14 shows the isometric and top views of the geometry to highlight the location and configuration of the impingement holes in the coolant domain. Jet impingement has been widely used in cooling solutions for steady and transient heat load applications. They are an extremely effective solution and are used widely in gas turbine cooling, laser and x-ray anode cooling, annealing, power electronics cooling etc [17]–[22]. Several different configurations were studied before choosing the current configuration in terms of spacing, jet diameter,  $l/d$  ratio etc. There is comprehensive literature available that discusses the effect of these parameters on cooling effectiveness and is therefore not being included in this discussion. The boundary conditions remain the same as the baseline case. The impinging jet diameter is chosen as 5 mm. The Figure 15 illustrates the flow of the coolant with streamlines.



(a) Isometric View

(b) Top View

**Figure 14: Two views to illustrate the location of impinging jets in the coolant domain.**

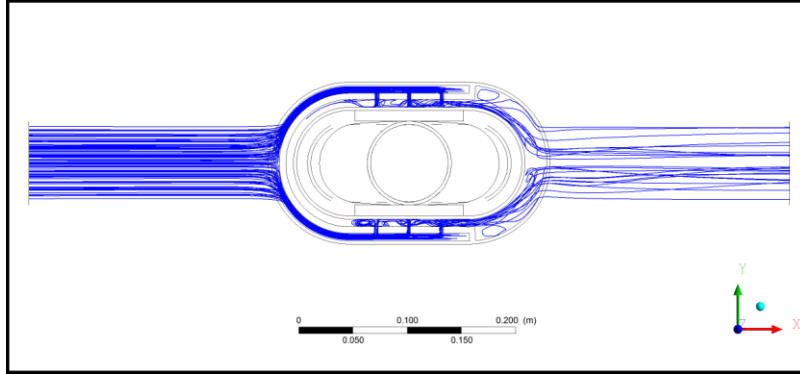


**Figure 15: Streamlines showing flow of coolant-Impinging Coolant Geometry**

Due to the presence of impinging jets, the temperature on the cold side of the modules is much more uniform. This is illustrated in Figure 16. Since the cold side now resembles a fixed temperature type boundary, the hot side temperatures fall gradually with increasing distance in the flow direction. The graph suggests the difference between the hot and cold side is higher than previous geometries. The average value of this difference is 190 °C

## **Comparison**

In order to highlight the difference and improvements between successive designs, Figure 17 plots the average hot and cold side temperature for each representative module and the temperature difference found across each module on the two sides. This clearly highlights the improvements made over the course of the design process. As can be expected, hot side temperatures are lowest for the impinging coolant geometry. However, the difference in temperatures is greatest for this case.

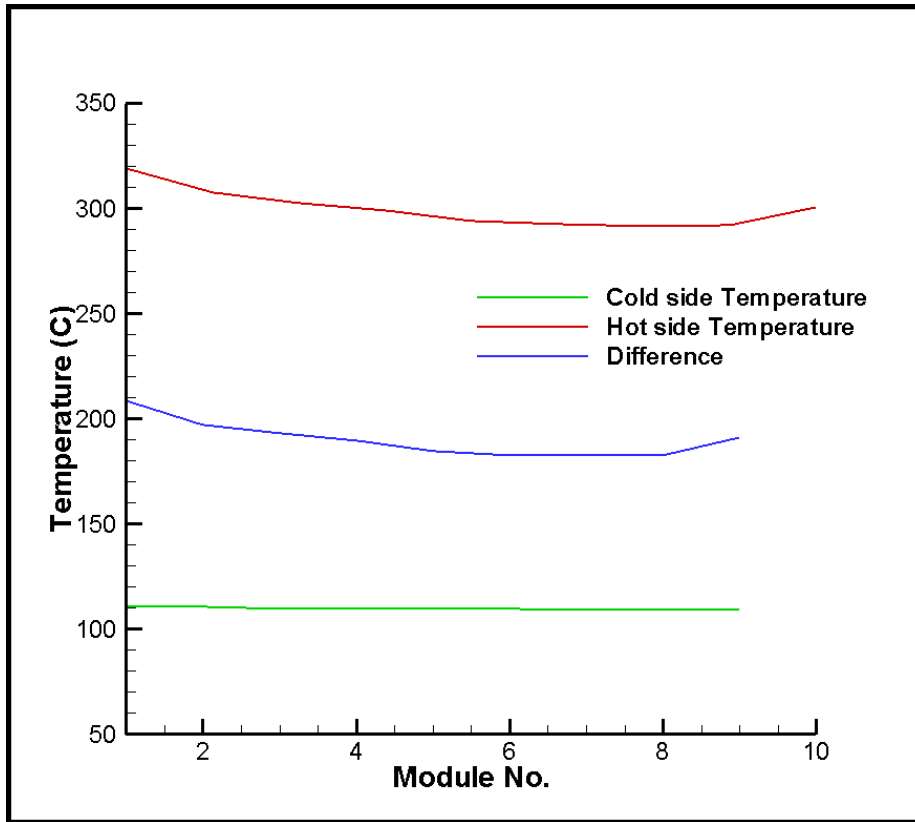
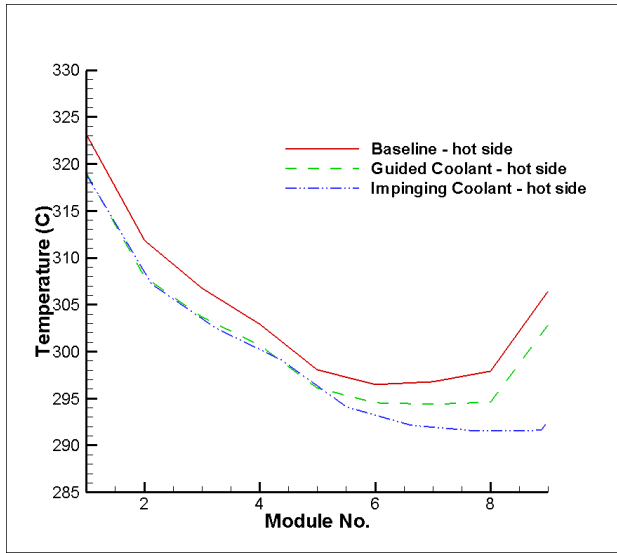
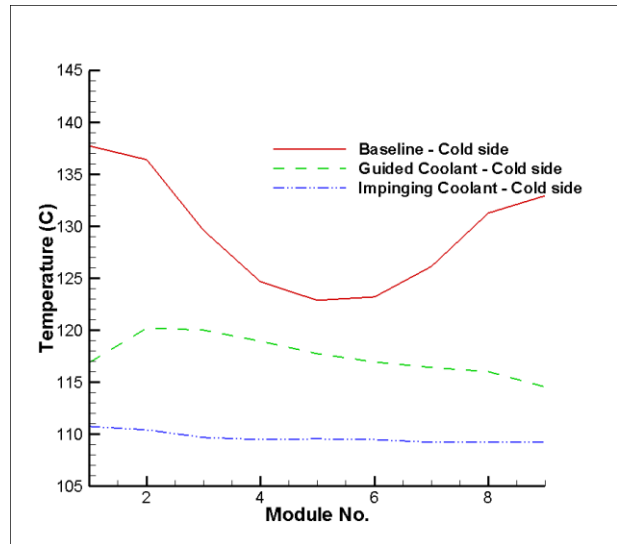


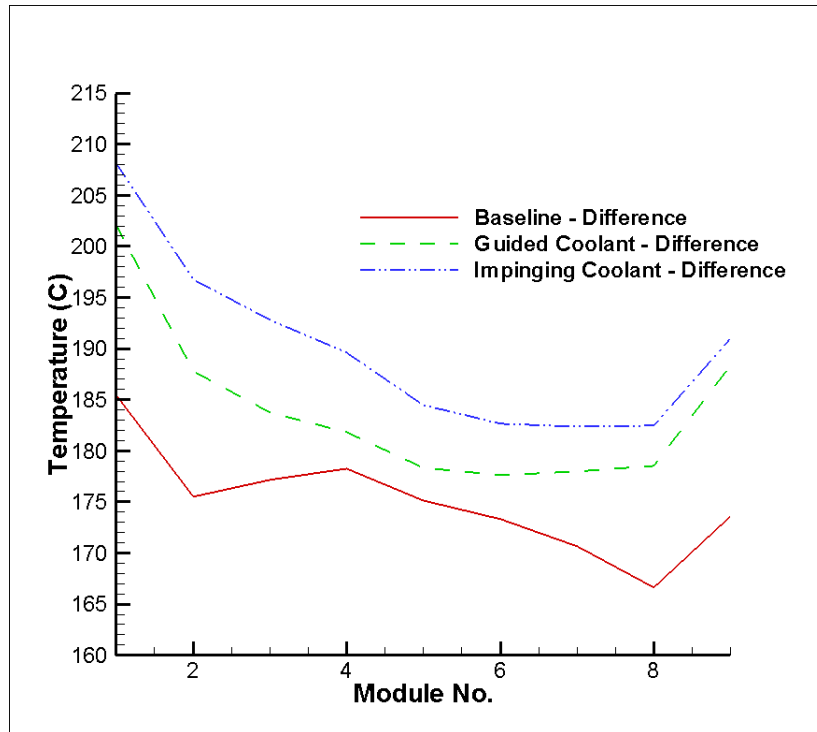
Figure 16: Plot for temperature difference (area averaged) across each module- Impinging Coolant Geometry



(a) Hot Side



(b) Cold Side



(c) Difference between temperatures ( $\Delta T$ )

Figure 17: Comparison of quantities of interest for the three cases.

## **Conclusion**

Three different heat exchanger designs were examined for a thermoelectric application to generate power from automobile exhaust gases. The designs were studied using CFD modeling and looking at overall temperature gradients across the thermoelectric modules. A typical baseline case was used for comparison. All design improvements are made on the coolant side of the heat exchanger. The data shows vast improvement in system response with every successive design. A design using jet impingement provides a significant increase in temperature gradient across the TEG module compared to a standard cross flow heat exchanger. The designs currently being examined employ heat transfer enhancement features on the hot loop of the heat exchanger also. This should improve the available temperature difference across the thermoelectric modules even more than the current configuration and result in higher power generation.

# **Chapter 3: Exhaust Gas Side Heat Transfer Enhancement**

## EXHAUST GAS SIDE HEAT TRANSFER ENHANCEMENT

In this chapter, the hot side of the heat exchanger is examined with the use of partial 3D internal pin fins to enhance heat transfer from the hot exhaust gases to the TEG. In order to limit pressure drop while maximizing the heat transfer, two factors are examined in pin fins: the cross sectional shape, and the pin fin height to channel height ratio. The investigation is performed using transient liquid crystal thermography.

A comprehensive literature survey of heat transfer enhancement using pin fins prior to 2000 is given by Han et al [23]. In 2009, Chyu et al.[24] investigated the performance index for various pin height to pin hydraulic diameter ( $h/D_{h-pf}$ ) ratios for pin fins, and they concluded that  $h/D_{h-pf}=2$  was the most favorable. The results from a similar study performed by Park et al. [25] concurred with results from Chyu et al.[24]. The hydraulic diameter and optimum spanwise and streamwise pitch for our current work are selected from a study by Siw et al.[26]. However, the present study investigates four different shapes (circular, triangular, hexagonal, diamond) at an  $h/D_{h-pf}$  ratio of 0.9. This ratio is selected based on a desired pin fin height ( $h$ ) equal to 15% of the total channel height ( $H$ ). The pin fin hydraulic diameter ( $D_{h-pf}$ ) is chosen based on the work by Chyu et al.[24]. The objective of this study is to provide usable data to compare heat transfer enhancement characteristics of various shaped pin fins at the chosen pin height to channel height ( $h/H$ ) and configuration. Once an optimum shape of the pin fins is chosen, the channel height is varied without changing any other parameters. This arrangement results in a variation in  $h/H$  while keeping the pin fin height to hydraulic diameter ( $h/D_{h-pf}$ ) ratio constant.

## Experimental Setup

A schematic diagram of the test section and test rig is shown in Figure 18. The setup allows for compressed air to enter from a 50-mm diameter pipe that expands to a 35.56-cm by 15.24-cm plenum. The 52-cm long plenum promotes a uniform velocity in the flow before passing through a mesh heater constructed of 304-stainless steel woven wire with a wire diameter of 20- $\mu$ m. A 5-cm spacer separates the mesh heater and the reduction nozzle leading to the test section to complete the test rig. Power is supplied to the mesh heater by a welding machine power source that provides low voltage, high amperage DC power.

The test section used to investigate the effect of cross section is shown in Figure 19. The pin fin height was chosen to be 15% of the channel height, and the test section is designed based on dimensions from the proposed heat exchanger described previously[27]. The inlet of the channel is 101.6-mm by 38.1-mm, and the plate length,  $L$ , is 254.0-mm. Each plate has an array of pin fins with hydraulic diameter,  $D_{h-pf}$ , of 6.35-mm. The streamwise pitch,  $S_{st}$ , is 12.7-mm with  $S_{st}/D_{h-pf} = 2$ , while the spanwise pitch is 22.23-mm ( $S_{sp}/D_{h-pf} = 3.5$ ) [25]. All plates are made from 12.7-mm thick plastic in order to ensure the validity of the semi-infinite solid assumption. The configuration for diamond pin fins is shown in Figure 20, and pin fins of all shapes are in the same staggered configuration. All geometries were studied at Reynolds numbers of 5,000 and 10,000 where Reynolds numbers are calculated based on the channel height and width, not accounting for the pin heights.

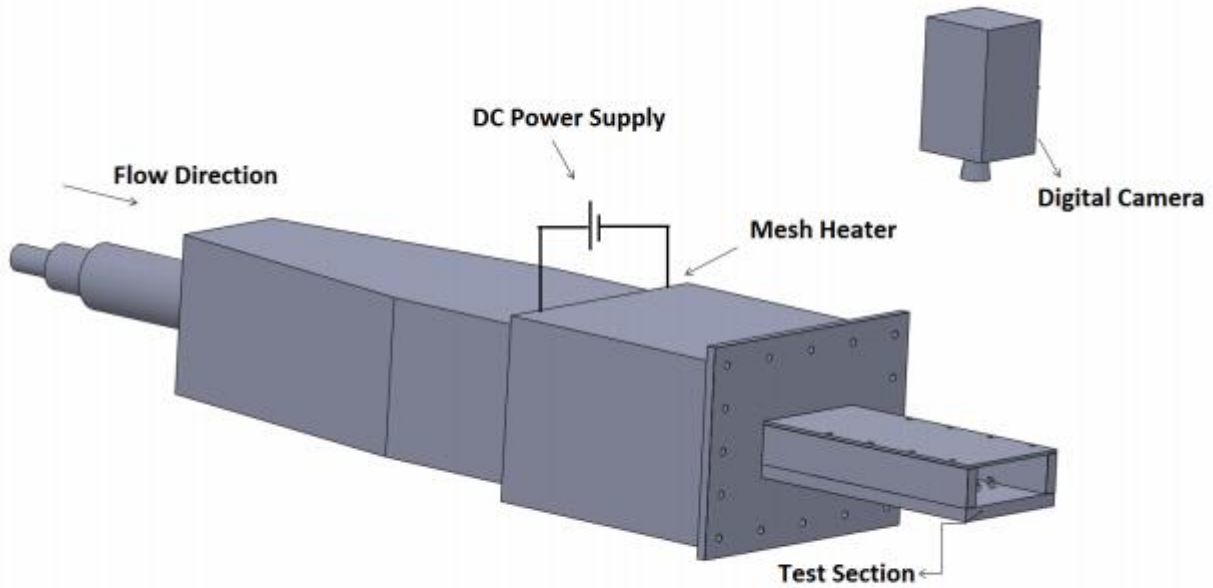


**Figure 18: Schematic of the test facility. The compressed air enters from the left, expands into a plenum before passing through a mesh heater and on into the test section.**

Once an optimum shape is selected, the channel height is varied in order to examine the effect of the  $h/H$  ratio on heat transfer. Figure 21 illustrates the test section for this analysis. The  $h/H$  ratio for the pins and channels is studied at two more values, 0.25 and 0.5 to determine the optimum performance based on this variation. For this experiment, the pin fin configuration on the plate remains the same as the previous tests.

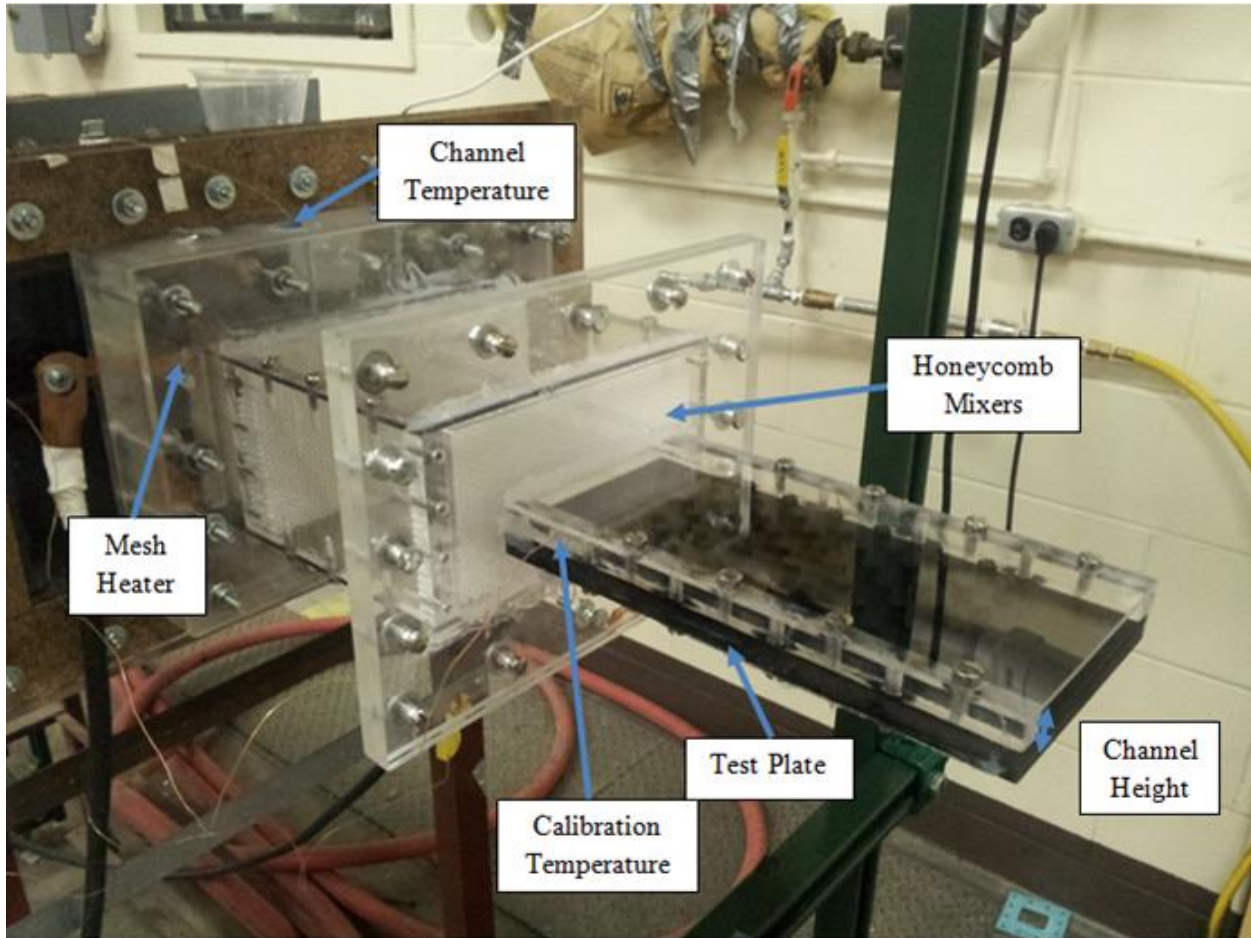


**Figure 19: Experimental test section. The compressed air enters from the left and is heated by the mesh heater before passing through the honeycomb mixers and on into the test section. The pin fins on the test plate are visible through the clear plastic in the test section**

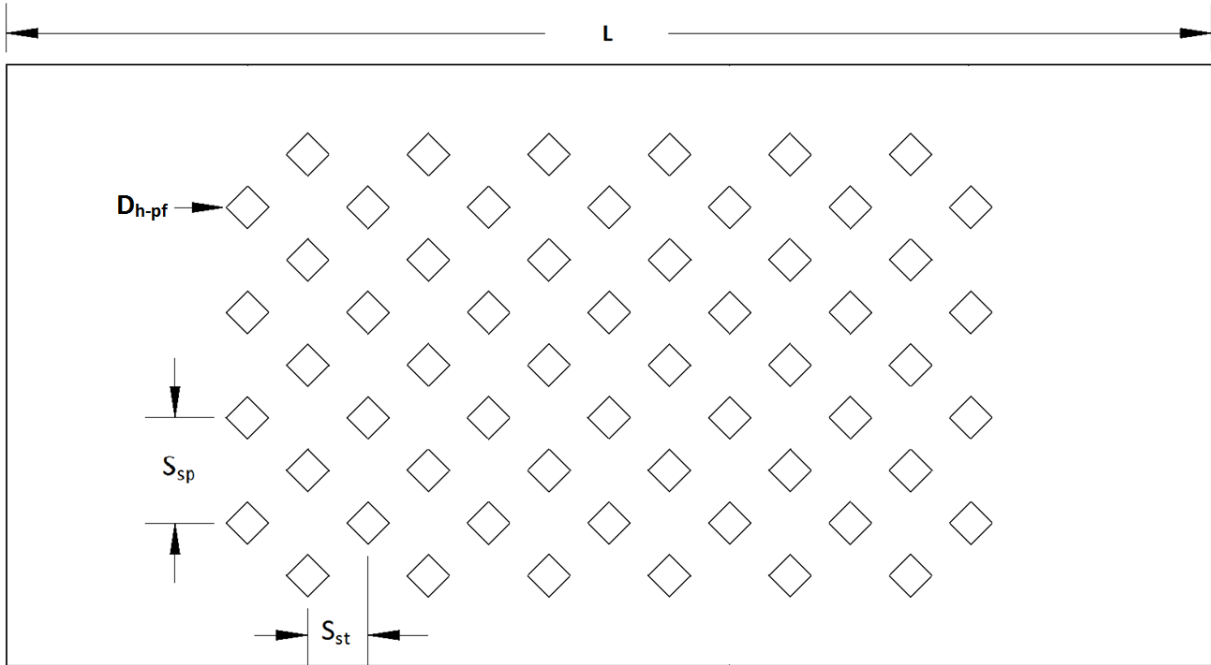


Figure 20: Top view of the pin fin configuration. The channel length,  $L$ , and the pin fin hydraulic diameter,  $D_{h-pf}$ , spanwise spacing,  $S_{sp}$ , and streamwise spacing,  $S_{st}$ , are labeled on the figure.

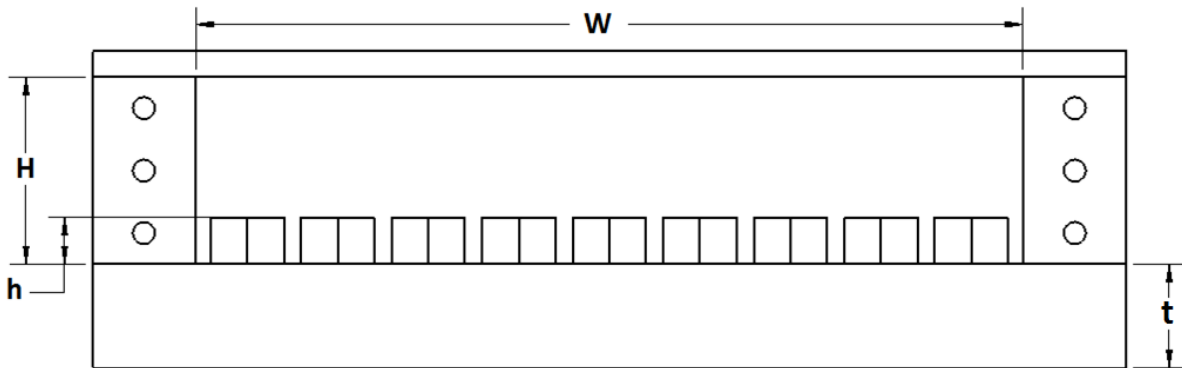


Figure 21: Front view of the test section. Here  $H$  is the channel height,  $h$  is the pin fin height,  $W$  is the channel width, and  $t$  is the thickness of the wall.

## Methodology

Compressed air is metered and enters through the inlet on the left side of Figure 18 and Figure 19. Orifice meters measure the mass flow rate of the air before the test section, and the pressure data from the orifice meters are collected with Omega PX-137 differential pressure transducers. The air then passes through a mesh heater which produces a change in temperature of the mainstream air,  $T_{ms}$ , in less than 33 ms after the heater is turned on [28]. Therefore, a step change in air temperature is assumed once the heater is turned on [29]. The mainstream temperature of the air,  $T_{ms}$ , and reference temperature on the test plate,  $T_w$ , is measured using Type K thermocouples. Temperature data are collected using an Omega OMB-DAQ-54 data logger. For each experiment, (a) video of the color change of the liquid crystal, and (b) the test plate temperature,  $T_w$ , as measured by the thermocouple, are simultaneously recorded. The starting times of the thermocouple data and the video are synchronized, and the thermocouple on the wall is used to calibrate the liquid crystal color with temperature by assigning the thermocouple temperature to a sample pixel area from the video that is located next to the thermocouple. The size of the pixel area is arbitrary, but set large enough to capture the true color change and to protect against random outliers. The thermochromic liquid crystals (R25C5W) used in this study have a temperature range of 25-30 °C. The light source is located next to the camera, so the maximum illumination angles are small.

The test section and test conditions were designed such that the system can be modeled as a semi-infinite solid with convection at the surface under transient conditions. This assumption is valid as long as the thermal penetration due to conduction does not extend all of the way through the material (causing 2-D conduction effects). The maximum allowable testing time where the 1-D semi-infinite solid assumption is satisfied is approximately 120 seconds given our plate

thickness and the low thermal diffusivity of ABS plastic. Our typical testing time is approximately 40-60 seconds, well below the maximum allowable time. Therefore, the semi-infinite solid assumption is valid (1-D conduction). With the semi-infinite solid assumption, the following relation is used to characterize the wall temperature ( $T_w$ )[30],

$$\frac{T_w - T_i}{T_{ms} - T_i} = 1 - \exp\left(\frac{(hct)^2 \alpha t}{k^2}\right) \operatorname{erfc}\left(\frac{(hct) \sqrt{\alpha t}}{k}\right) \quad \text{Equation 3}$$

where  $T_i$  is the initial wall temperature of the test section at time  $t = 0$ ,  $T_{ms}$  is the bulk temperature of the airflow entering the test section after the heater,  $\alpha$  is the thermal diffusivity of the test section material (ABS),  $t$  is the time of the color change,  $hct$  is the heat transfer coefficient, and  $k$  is the thermal conductivity of the material (ABS). Properties were evaluated based on the average of  $T_{ms}$  and  $T_w$ . The bulk temperature and the initial wall temperature are measured with thermocouples. In this equation, all quantities are known except for  $hct$  and  $T_w$ . The wall temperature,  $T_w$ , at every location is determined from the liquid crystal color change after calibrating the liquid crystal color with the wall reference temperature as measured by the thermocouple.

### Wall Temperature Calculation

The measurement of the surface temperature during the transient test is required in order to calculate the heat transfer coefficient from Equation 3. The wall temperature is determined using the video of the color change of the liquid crystal using the hue calibration method.

In the hue calibration method, the color data from the video of the liquid crystal color change is converted from red, green, and blue (RGB) to the hue saturation value (HSV) scale. Next, the thermocouple recorded wall temperatures are used to calibrate the hue values recorded for pixels adjacent to the thermocouple location. The thermocouple data is combined with the hue recorded around the calibration thermocouple to develop a calibration curve as a function of time as shown in Figure 22. Each test is recalibrated to prevent error from liquid crystal degradation over time or any other non-uniformity between measurements. The resulting equation from the curve fit must have an  $R^2$  value greater than 0.9, indicating a strong linear correlation of the data set. The resulting equation is used to equate hue to temperature for every pixel at every frame, thus the time variation of temperature at each pixel is observed. Each pixel has a unique change in temperature, therefore a unique heat transfer coefficient.

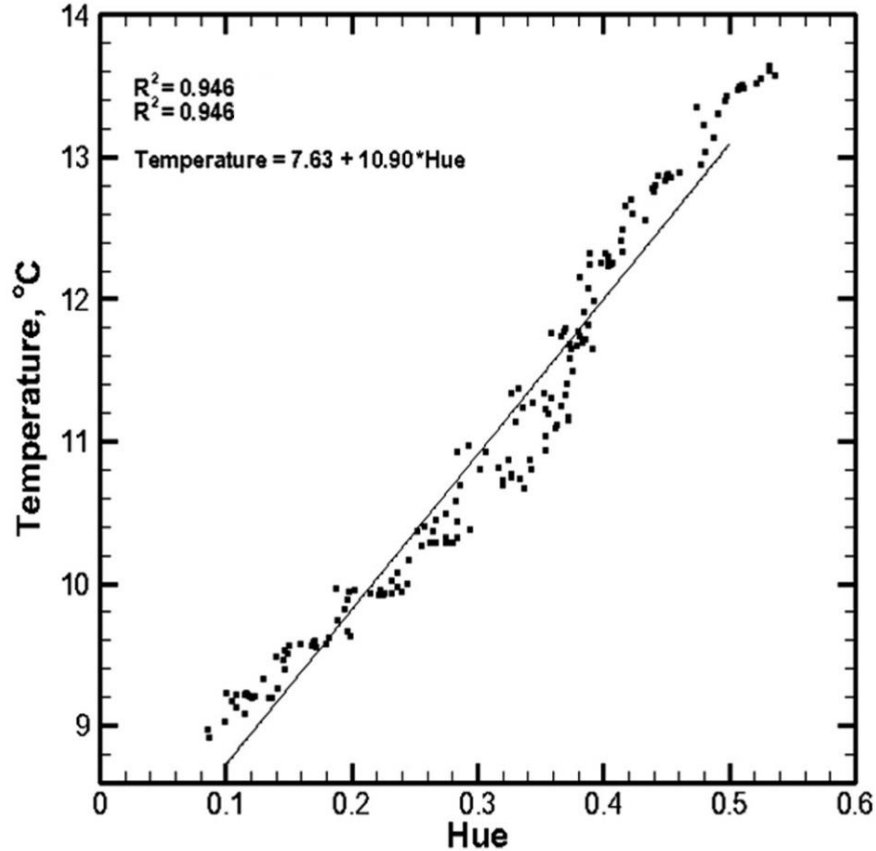


**Figure 22: Typical calibration curve for the Transient Liquid Crystal (TLC) measurements. The temperature is measured by a reference thermocouple on the wall, and the hue is recorded on the area adjacent to the thermocouple location on the wall. The near linear relationship between the measured temperature and the hue is used to calibrate the temperatures at other locations on the test surface.**

Once the wall temperature,  $T_w$ , is determined for every pixel on the surface as a function of time, the heat transfer coefficient,  $h_{tc}$ , is the only remaining unknown in Equation 3. Theoretically, only one wall temperature measurement at a known time is needed to solve the equation for the heat transfer coefficient. However, in order to reduce errors, data are collected over the liquid crystal color range for the test duration in the hue calibration method. We then use a regression analysis to reduce random errors in recorded local wall temperatures over a range of up to 30

seconds of data at 30 frames per second. The regression analysis puts all terms of the conduction equation (Equation 3) on the right hand side of the equation, which is then solved for all times at each pixel. This analysis results in a residual error for each time-temperature data pair. The residual error is minimized with a least squares method by solving for the heat transfer coefficient that best fits all data. By examining the data as a function of time the random camera read errors (due to lighting variations) of the liquid crystal paint are reduced, and this approach also relaxes the dependence on the initial temperature of the target plate. Figure 23 illustrates the relatively constant nature of the heat transfer coefficient over a span of approximately 10 seconds. Once the convection heat transfer coefficient is determined, the Nusselt number,  $Nu$ , is calculated from

$$Nu = \frac{(htc) D_{h-ch}}{k} \quad \text{Equation 4}$$

where  $htc$  is the local convection heat transfer coefficient,  $D_{h-ch}$  is the hydraulic diameter of the channel, and  $k$  is the local thermal conductivity of the air.

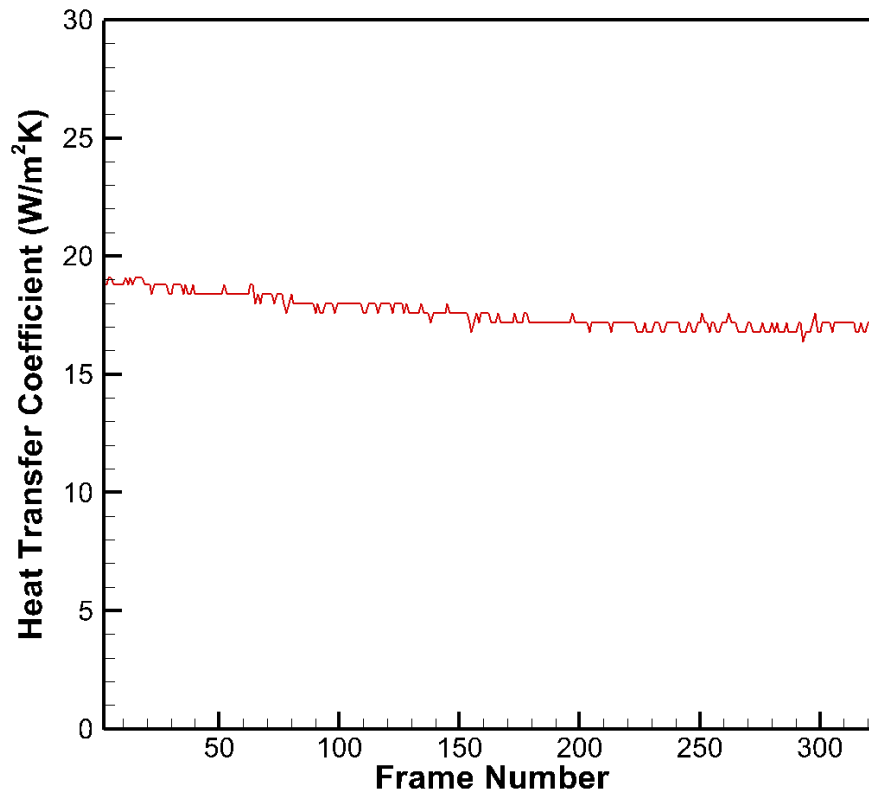


**Figure 23: Heat transfer coefficient as measured with the transient liquid crystal technique. The measurements were recorded at 30 frames per second, so the plot covers approximately 10 seconds of time. The relatively constant heat transfer coefficient results demonstrate the stability of these measurements.**

All experimental data is post processed by the green start technique as well to reduce uncertainty. In this method, the calibration thermocouple is used to find a temperature corresponding to the appearance of green on the surface. Then the time taken for each pixel to reach this color is stored in a matrix. This gives the different times taken for each pixel to reach the calibration temperature. This results in a constant  $T(0,t)$  at every pixel in Equation 3 but each pixel has a different time associated with that temperature. This technique is much faster than the hue

calibration method but has a greater uncertainty associated with it. Therefore it is used only to introduce redundancy and improve the accuracy of the solutions.

## **Uncertainty**

Uncertainty in the heat transfer coefficient,  $h_{tc}$ , is determined by evaluating the individual uncertainties in the measurements following the methods outlined by Kline and McClintock [31]. The measurement uncertainty in the initial, mainstream and wall temperatures are ( $T_i$ ,  $T_{ms}$ , and  $T_w$ ) all 1.0 °C, while the uncertainty in the camera shutter speed is approximately 17 ms [32]. The overall uncertainty in the heat transfer coefficient is then calculated to be  $\pm 7.5\%$ .

## **Results & Discussion**

In this section, results from the experiments for different pin fin configurations with a Reynolds number range of 5,000 – 20,000 are presented. Two-dimensional contour plots of the heat transfer coefficient on the test surface provide insight into the influence that the pin fins have on heat transfer from the air to the solid. Spanwise averaged heat transfer coefficients and area average heat transfer coefficient data provided in the form of the Nusselt numbers are also reported.

Figure 24 displays contour plots of the heat transfer coefficients for four different pin fin geometries. As can be seen from the contours, the diamond shaped pin fins reduce flow separation around the pin, thus improving heat transfer in the area immediately behind each fin.

The triangular and hexagonal pin fins promote flow separation behind the pins causing large areas of low heat transfer which result in a lower overall heat transfer coefficient. As expected, the heat transfer coefficient reduces in the flow direction due to the increasing boundary layer thickness. The streamwise length scale in the figure is  $l/L = 0.8$ , where ' $l$ ' is the variable in the streamwise direction and ' $L$ ' is the total length of the plate.

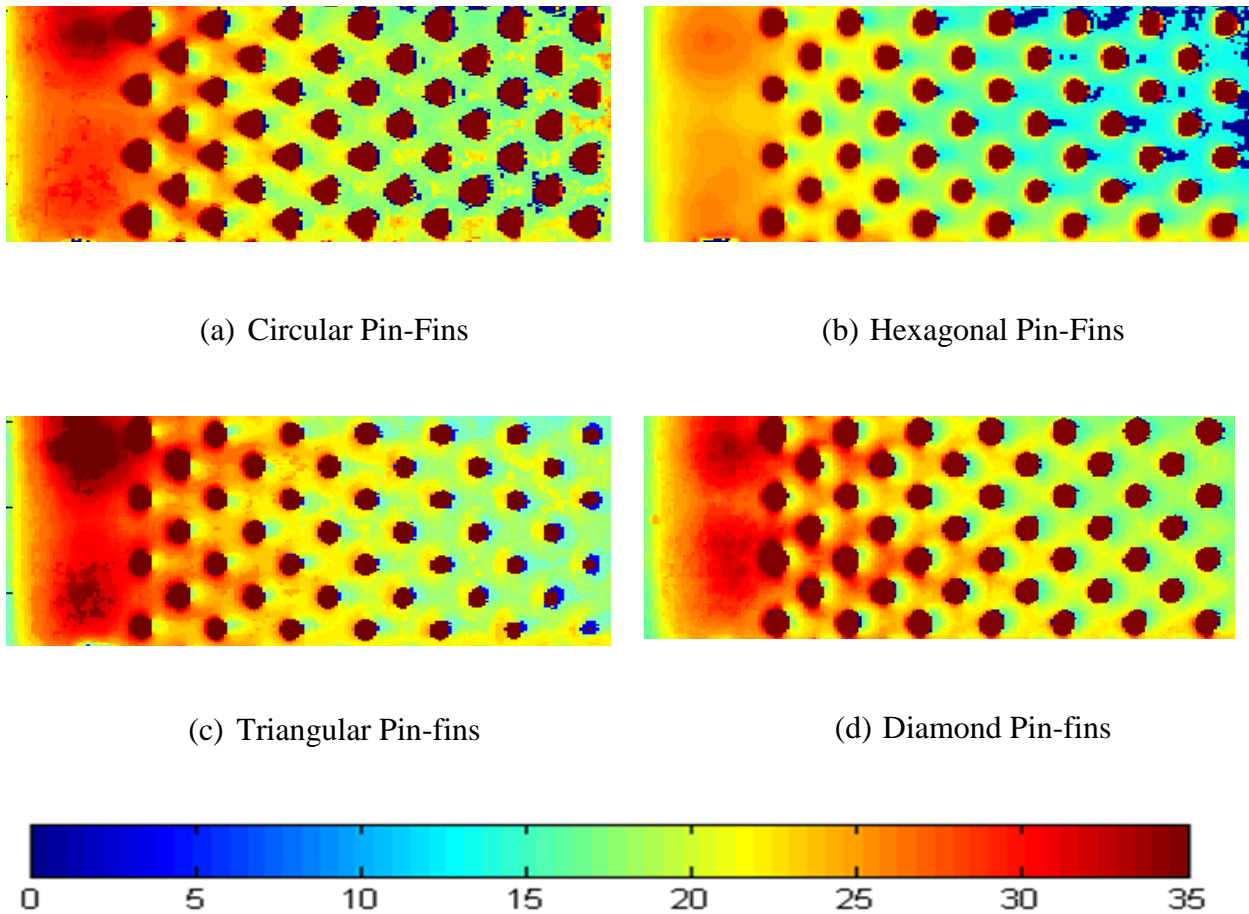


**Figure 24: Heat transfer coefficients for various pin fin shapes as measured by the transient liquid crystal technique at a Reynolds number of 5,000. The local heat transfer coefficient is keyed to the color according to the scale below the images in units of  $W/(m^2-K)$ , and the air flow direction is from the left to right. We find that the diamond shaped pin fins give the best heat transfer enhancement, as  $h_{tc}$  is larger throughout the length of the test specimen. Image resolution is limited by experiment.**

Spanwise averaged Nusselt numbers are plotted in Figure 25(a) and Figure 25(b), normalized against experimental data from a baseline case with a duct without any enhancement features ( $Nu_0$ ), for Reynolds numbers of 5,000 and 10,000, respectively. The streamwise distance,  $x$ , is normalized against the hydraulic diameter of the channel. The plots show the effect of the entrance region up to  $x/D_{h-ch} = 0.6$ . The pin fins contribute in enhancing the heat transfer after  $x/D_{h-ch} = 0.6$ . It is clear from Figure 25(a) that diamond pin fins provide the greatest improvement in heat transfer for  $Re = 5,000$  consistent with the findings in the contour plots shown in Figure 24. However, for  $Re = 10,000$ , the difference between the diamond fins and circular and triangular fins diminishes. The relative insensitivity of the heat transfer to these shapes may largely be a result of the higher baseline heat transfer coefficients at the higher Reynolds number. The additional turbulence caused by the pin fins is smaller compared to the inherent turbulence of the flow at the larger Reynolds number. Thus, fin geometries have a smaller impact on the heat transfer characteristics of the system at higher Reynolds numbers as compared to lower Reynolds numbers. The hexagonal pin fins are an exception as the normalized Nusselt number for this geometry is considerably less than the other three shapes at  $Re = 10,000$ . The hexagonal shapes may promote flow separation around the pin fins which results in a low flow region immediately behind the pin fins, thus limiting the heat transfer enhancement. Thus there is virtually no change in the heat transfer enhancement for the hexagonal pin fins when the Reynolds number increases from 5,000 to 10,000.

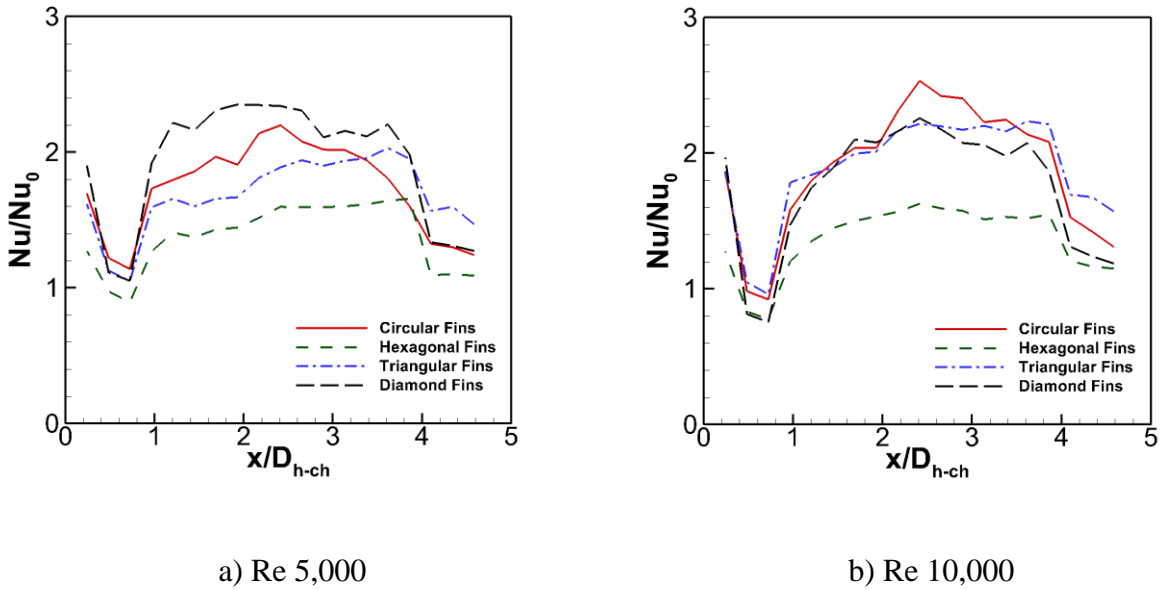


**Figure 25: Spanwise area averaged normalized Nusselt numbers for Reynolds numbers of (a) 5,000, and (b) 10,000. The diamond pin fins are superior at Re = 5,000, but for Re = 10,000 the circular, hexagonal, and triangular pin fins give nearly the same results. For both Reynolds numbers, the hexagonal pin fins have the smallest heat transfer due to large flow separation around the pins.**

Figure 26 displays comparisons of the area averaged Nusselt number normalized by the heat transfer data from the examined flat plate for Reynolds numbers of 5,000 and 10,000 for all cases. The Nusselt number from the baseline case is greater than the fully developed flow Nusselt number derived from the Dittus-Boelter equation (for fully developed flow) (Equation 5) by a factor of two.

$$Nu_D = 0.023 Re_D^{4/5} Pr^{0.3} \quad \text{Equation 5}$$

This difference can be attributed to the fact that the length of the test section does not allow the flow to become fully developed in the region where the pins are placed. Therefore, the entrance region in the measurement increases the area averaged heat transfer significantly as compared to the Dittus-Boelter equation. Consistent with our earlier findings, the area averaged Nusselt number confirms that the diamond shaped pin fins do give the greatest enhancement in heat transfer at both Reynolds numbers, although the triangular and circular pin fins give nearly the same improvement at  $Re = 10,000$ . The enhancement is significant as the short pin fins with  $h/H = 0.15$  increase the area averaged Nusselt number by a factor of  $\sim 1.9$  as compared to the baseline case without any enhancement features.

From the previous results, it is clear that the diamond shaped pin fins perform the best with respect to heat transfer enhancement. Therefore, this shape is further examined for the effect of the pin fin height with respect to the channel height, i.e. the  $h/H$  ratio, on heat transfer in the test section. Figure 27 shows the contour plots for the heat transfer coefficient distribution on the pin fin surface with two channel height ratios, 0.25 and 0.5. For the same Reynolds number, the fluid velocity through the narrower channel is higher than for the wider channel. Also, the pin fins form a more significant blockage in the narrower channel as compared to the wider channel. It is therefore clear that the effect of pin fins in the narrower channel is to increase the channel flow velocity for the same Reynolds number with a reduction in channel hydraulic diameter and thus provides significantly higher heat transfer coefficients. This is observed for all Reynolds numbers. The same trend can also be observed in the area averaged results as shown in Figure 28. There is a significant increase in heat transfer coefficients between the  $h/H = 25\%$  channel and the  $h/H = 50\%$  channel.

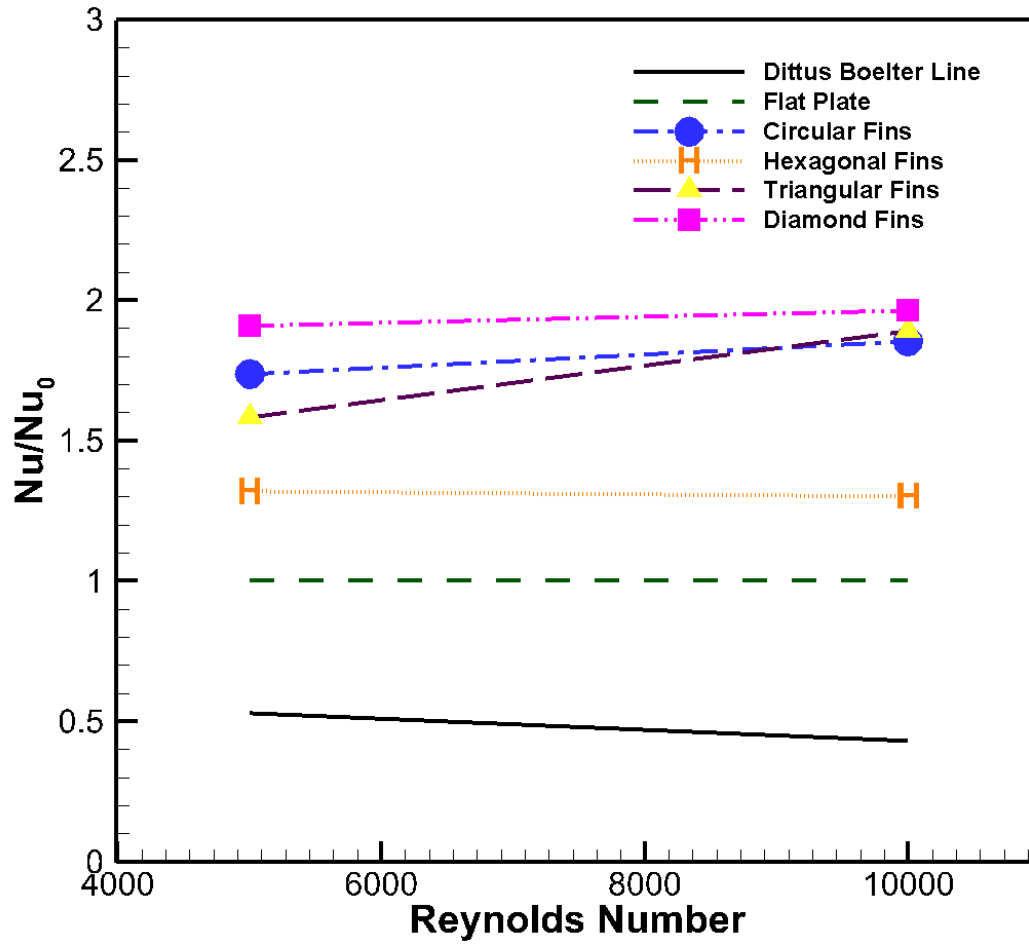
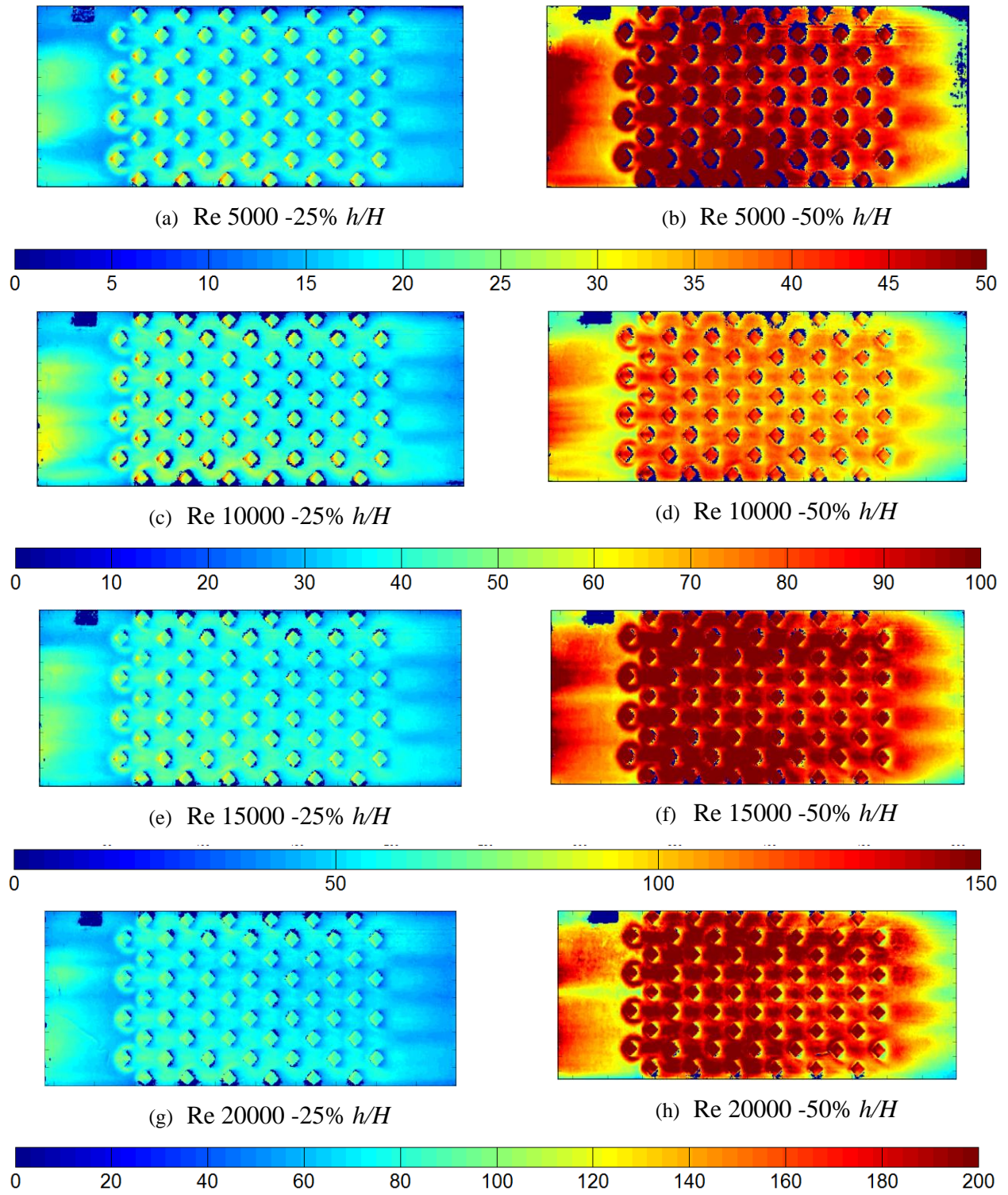
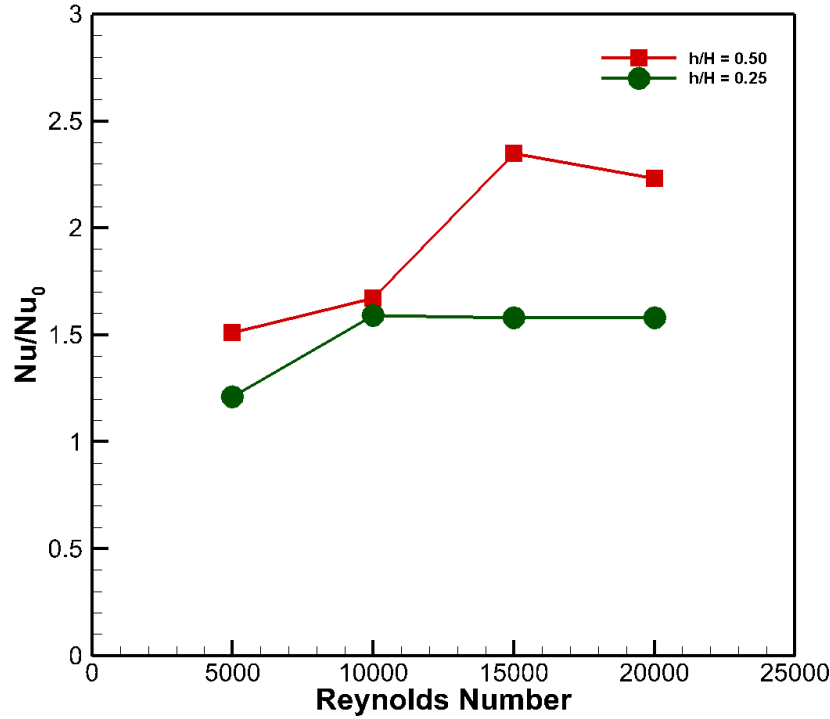


Figure 26: Normalized Nusselt number for the different pin fin shapes at Reynolds numbers of 5,000 and 10,000. Here the Nusselt number is averaged over the area that begins with the entrance to the test section, and ends with the last row of the pin fins (i.e. the same area as shown in Fig. 7). Again, the diamond shaped pin fins display the greatest enhancement in heat transfer.



**Figure 27: Heat transfer coefficient distribution with varying Reynolds number and  $h/H$  ratios for diamond shaped pin fins.**



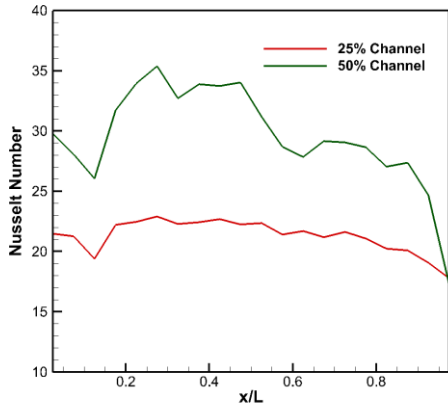
**Figure 28: Normalized Area Averaged Nusselt number for different pin fin heights as a function of Reynolds number. The effect of pin fin height to channel height ratio ( $h/H$ ) on heat transfer enhancement ( $Nu/Nu_0$ ) is shown here.**

Area averaged heat transfer coefficients are represented in terms of Nusselt number, as defined in Equation 4. The Nusselt number is then normalized with  $Nu_D$ , obtained using the Dittus-Boelter equation for flow over a flat plate given by equation 3. It is important to note that the baseline Nusselt number ( $Nu_0$ ) is a measured quantity for the plate with no pin fins whereas the Dittus-Boelter correlation is for the fully developed Nusselt number value at the same Reynolds number. The results are plotted in Figure 28, and show that the improvement in heat transfer performance is greater for the case with the narrower channel. The results also indicate that the improvement increases with increasing Reynolds number before leveling out in the high Reynolds number regimes.

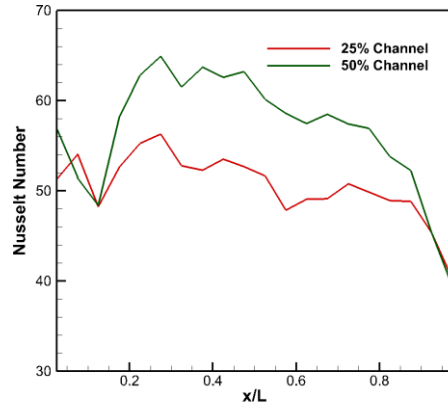
Spanwise area averaged Nusselt numbers are plotted at four different Reynolds numbers in Figure 29. These plots show that the Nusselt number is high at the entrance region as expected and steadily drops until it reaches  $x/L = 0.2$ . After this point, the pins trip the growing boundary layer and the Nusselt number increases again up to  $x/L = 0.8$ .

Since these Nusselt numbers are area averaged with the pins enclosed in continuous areas, these plots do not highlight the effects of individual rows of pins. In order to show the effects of the individual rows of pins, the spanwise line averaged Nusselt numbers are plotted as a function of non-dimensional distance in Figure 30. The peaks observed in these plots occur on top of the pin fins, while the valleys are located between two rows of pin fins. There are 14 rows of pin fins in the test section and each row clearly creates a peak in the data as shown in Figure 30. However, at lower Reynolds number and 50%  $h/H$  ratio, the effect of the first row of fins is less pronounced. The peaks increase in intensity steadily from  $Re = 5,000$  (Figure 30(a)) to  $Re = 20,000$  (Figure 30(d)). The increased blockage at lower Reynolds numbers results in higher heat transfer downstream.

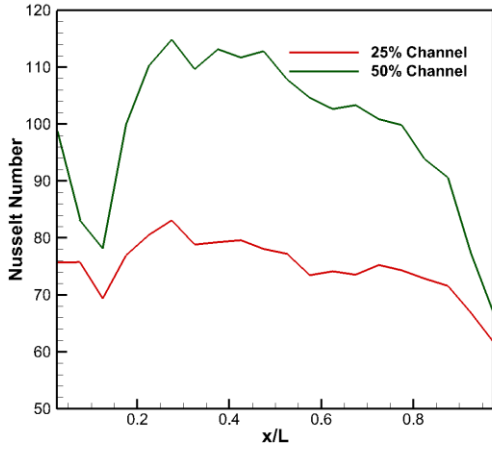
Diamond shaped pin fins provided the best overall heat transfer enhancement. The improved performance of the diamond pin fins is due to the fact that, unlike other shapes, they minimize flow separation caused around the fin and therefore have a much smaller low heat transfer region immediately behind them. The staggered configuration also promotes flow in these low flow regions by guiding oncoming flow into these areas. This nature of diamond shaped pin fins also provides lower pressure drop than other shapes which was very low for all cases and thus could not be measured.



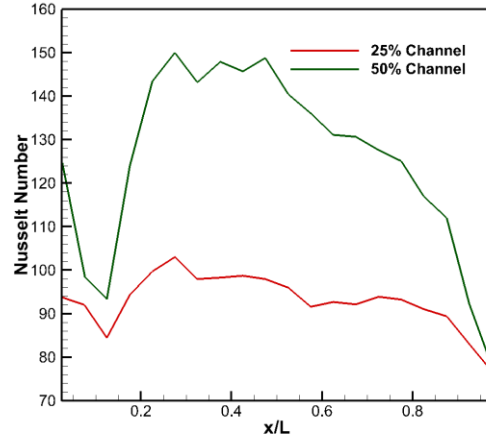
(a) Re 5000



(b) Re 10000

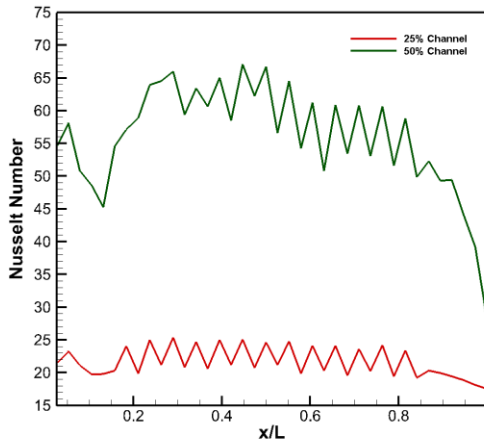


(c) Re 15000

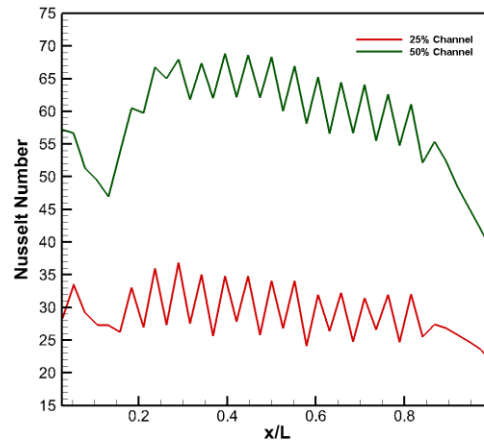


(d) Re 20000

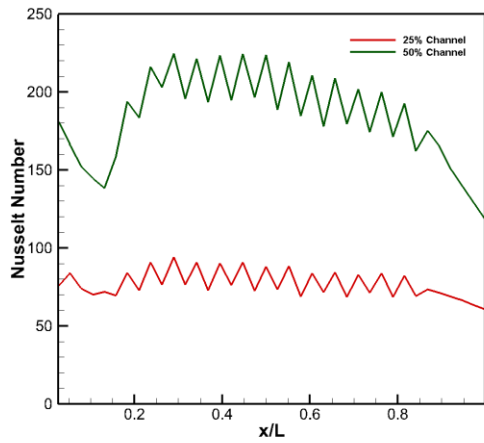
**Figure 29: Spanwise area averaged normalized Nusselt numbers for different Reynolds numbers with varying  $h/H$  ratios. The average is calculated over an area enclosing the fins.**



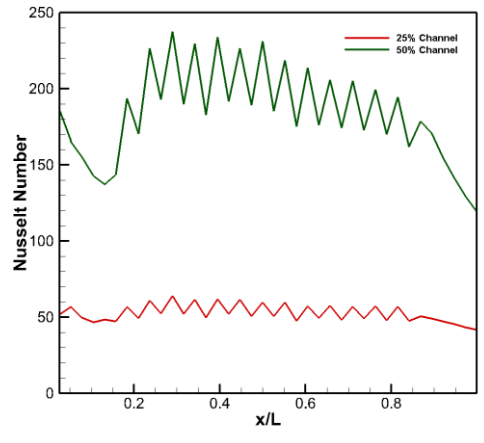
(a) Re 5000



(b) Re 10000



(c) Re 15000



(d) Re 20000

**Figure 30: Spanwise line averaged normalized Nusselt numbers for Reynolds numbers between 5,000 and 20,000 and  $h/H$  ratios of 25 % and 50 %.**

## Conclusions

Heat transfer enhancement methods were evaluated in order to improve the performance of thermoelectric power generators in automotive applications. Specifically, pin fin geometries were examined in a fixed configuration array at pin heights that ranged between 15 % and 50 % of the channel height. The results indicate that diamond shaped pin fins gave the greatest

enhancement in heat transfer when compared with other shapes. The study also evaluated heat transfer enhancement characteristics with varying fin height to channel height ratio while maintaining a constant hydraulic diameter. Data from these experiments show that maximum heat transfer is achieved when the pin fin to channel height ratio is 0.5. The pressure drop caused by the pin fins is small since they do not extend fully into the flow path and hence could not be measured. Thus these pin fins can be used without an adverse effect on the vehicle in terms of back pressure in the exhaust tailpipe.

By implementing the examined partial pin fins in the exhaust gas path, the heat transfer from the exhaust gas to the TEG can be significantly improved, in turn increasing the power output from the system. This work demonstrates that pin fin height, shape, configuration and height as compared to the channel are important parameters to consider while designing the heat exchanger for the exhaust tailpipe.

**Chapter 4: Experimental Investigation of Heat Transfer in  
Thermoelectric Generator for Automotive Exhaust Waste Energy  
Harvesting.**

## **EXPERIMENTAL INVESTIGATION OF HEAT TRANSFER IN THERMOELECTRIC GENERATOR FOR AUTOMOTIVE EXHAUST WASTE ENERGY HARVESTING.**

The focus of this study is to demonstrate heat transfer enhancement geometries on heat exchangers to enhance the temperature gradients across a thermoelectric generator (TEG) and further improve efficiency of waste heat energy harvesting. The heat exchanger uses the tailpipe exhaust gases from a vehicle as a heat source and the radiator coolant as the cold sink. Different heat transfer enhancement features are employed on the cold side and the hot side of the device to achieve as large of a temperature gradient as possible. Various flow Reynolds numbers and inlet temperatures are examined to create a database of predicted total power output from the TEG. Results are normalized against the output for baseline heat exchanger designs that have no heat transfer enhancement geometry. The experiments are carried out at 1/5th scale of the actual engine scale geometry. Impinging jets are employed on the coolant side while pin fins are used on the hot gas side for maximum heat transfer enhancement. The experimental test sections are fabricated using metal 3D printing. Water is used instead of radiator coolant and heated air is used for exhaust gases.

### **Experimental Setup**

The design of the heat exchanger for this study was built around a flattened section of the exhaust tailpipe. The top and bottom of the pipe are flattened so that pre-manufactured TEGs can easily and inexpensively be mounted on the tailpipe. The flattened pipe has more cross sectional area, causing the exhaust flow to slow down and, as a result, transfer heat more efficiently by increasing residence time. The engine coolant loop present in the car will be extended to provide

cooling to the TEG. Figure 31 shows the layout of the proposed heat exchanger at full scale, while Figure 32 shows the front view of the section.

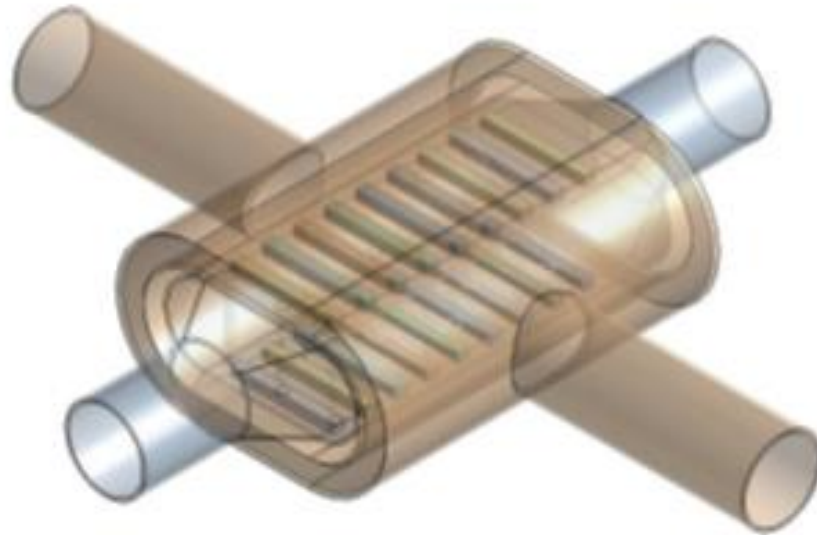


**Figure 31: Layout of the baseline heat exchanger. The exhaust gas travels from the lower left of the system through the heat exchanger and exits at the top right. The coolant flows from the top left through the pipe and exits at the bottom right. The rectangular pieces inside represent sample TEGs. (Pandit et al [33])**

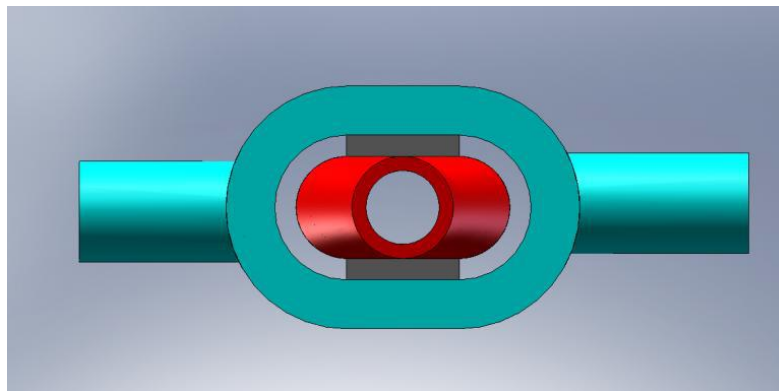


**Figure 32: Front view of the layout of the heat exchanger. The coolant flows from left to right around the outside of the system, while the exhaust gas flow is normal to the page in the center of the device. The TEG is secured in between the hot and the cold sides of the heat exchanger.**

In the current study, the purpose of the test section is to measure the temperature gradient across the TEG module. This study does not measure the total system energy output, thus a scaled down set-up was acceptable. The system is scaled down to 1/5<sup>th</sup> of the size of an actual device that would be used in an automobile. It is scaled geometrically using the Reynolds Number, and fluid flow rates are also scaled down to match the Reynolds numbers. The operating temperatures remain the same as would be expected in actual exhaust and coolant flows.

The TEG module has a hot side and a cold side, thus requiring a hot loop and a cold loop. The hot loop in the CFD model uses 400 °C air, based on the temperature of exhaust gas after exiting the catalytic converter in the tailpipe of a typical sedan [3], [34]. The Reynolds numbers in each loop were calculated based on 3000 rpm operation of a 3-liter engine. The hot loop has air with a volumetric flow rate of 0.0151 m<sup>3</sup>/s through a pipe with diameter of 0.013 m, and the cold loop runs at 3.15x10<sup>-5</sup> m<sup>3</sup>/s through tubing with a diameter of 0.013 m. In order to quantify changes in the system, results from a baseline case are compared with various heat exchanger configurations. The baseline case is the simplest configuration with no heat transfer improvement features located in the path of the flow. These baseline measurements allow us to quantify the improvement in heat transfer behavior with the enhancement features.

## **Test Section**

The actual heat exchangers tested were manufactured by ExOne, which is a digital part materialization company, using a metal additive manufacturing process. The test section was printed in two pieces (hot and cold sides) using a mix of 420-stainless steel and bronze. Printing ensures that the details and features of the designed sections are maintained, providing exactly

the same part as the one used previously (Pandit et al. [33]) without the need for assembly. Figure 33 and Figure 34 show pictures of the manufactured hot and cold side baseline geometry sections. The specified roughness average (Ra) of the baseline parts was  $1.25\ \mu\text{m}$  on the outside surfaces and  $7.5\ \mu\text{m}$  on the inside surfaces of the part. Tolerances were quoted to be  $\pm 0.13\ \text{mm}$  ( $0.005''$ ).

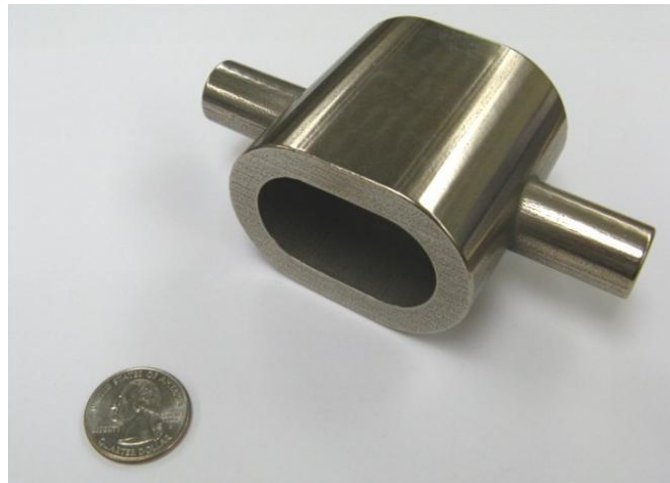


**Figure 33: Cold side baseline geometry test section piece. This piece is 58 mm x 108 mm x 43 mm.**



**Figure 34: Hot side test section piece. This piece is 73 mm x 38 mm x 18 mm.**

Two separate cold side geometries were manufactured: one without enhancement features and one with holes for impingement jets. The internal features of the two cold side sections are

illustrated in Figure 35, Figure 36a, and Figure 36b. The two cold side geometries differ on the inside of the section piece, in the flow path. The baseline geometry is simply a pipe that opens into an open section around the hot side piece, as seen in Figure 35. The impingement geometry is more complicated. As seen in Figure 36a and Figure 36b, the flow moves in one pipe and it hits a wall on the far side of the flat section of the cold side. This wall forces the flow through the impingement holes in the flat section. This flow is pushed out through the second pipe.

Similarly, two separate hot side geometries were also manufactured, one with and the other without heat transfer enhancement features. As seen in Figure 34, the baseline hot side geometry is a flattened section of the tailpipe which helps to slow down the flow and improves residence time and also increases wetted surface area. The second geometry implements diamond shaped pin-fins that have been previously experimentally studied and shown to have the best heat transfer performance [35], [36] The configuration and extent of the pin-fins is also chosen based on the previous studies conducted by Pandit et al. This geometry can be seen in Figure 37.

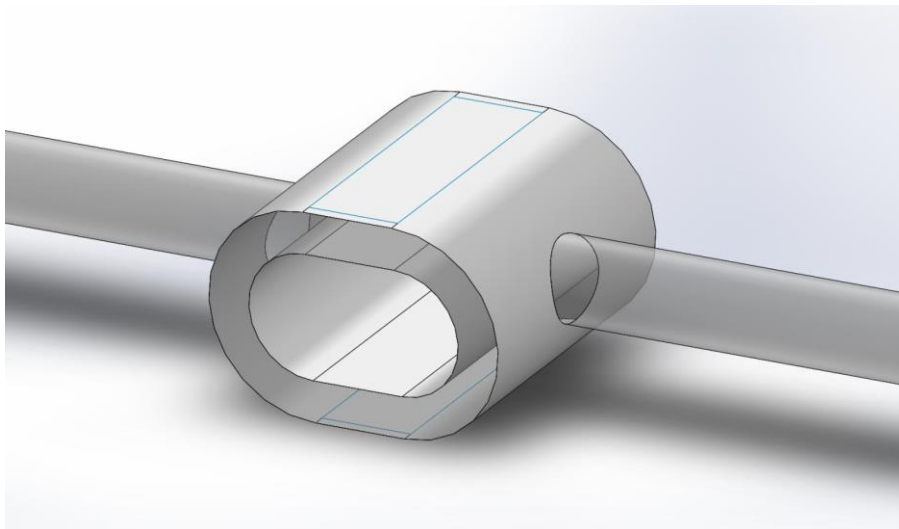
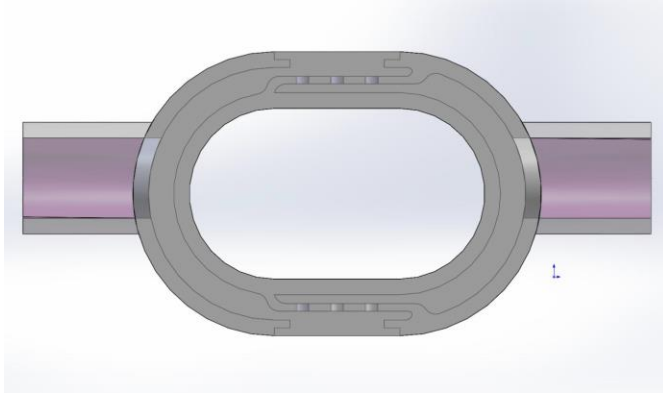
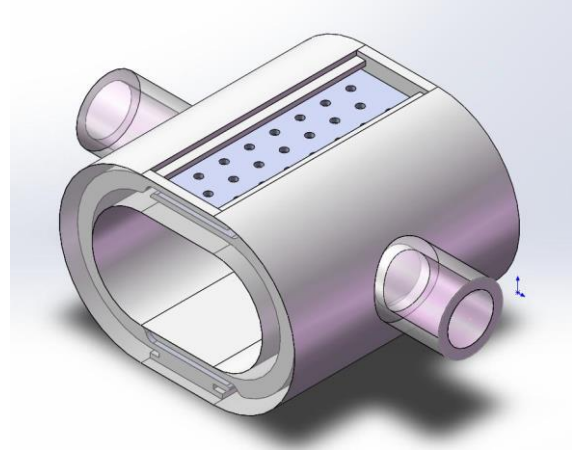


**Figure 35: Cold side baseline geometry**



a) Front View



b) Isometric View

**Figure 36: Cold side impingement jet geometry**

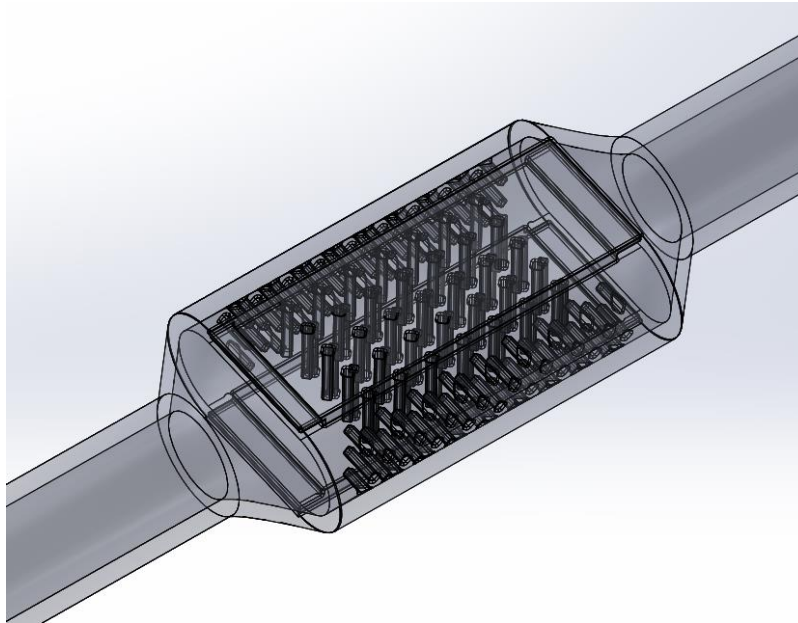


**Figure 37: Exhaust side pin-fin geometry**

## Test Matrix

In order to be able to predict power output through a thermoelectric system harnessing the exhaust energy from a car based on different driving and traffic conditions, the experiments are carried out in a variety of test conditions. The heat transfer enhancement is examined by varying inlet flow rates for the hot air, inlet temperature for the hot air and inlet flow rate for the coolant. This results in a total of 72 test cases. However, due to limitations in the experimental rig, certain cases conditions could not be achieved, like high temperature at high inlet flow rates for the exhaust air. Table 2 illustrates all of the test cases that were examined with repeatable results.

In the test matrix, the various exhaust flow rates represent different operating RPM of the engine at full scale.  $0.0118 \text{ m}^3/\text{s}$  corresponds to 2360 RPM,  $0.0095 \text{ m}^3/\text{s}$  to 1900 RPM and  $0.0047 \text{ m}^3/\text{s}$  to 950 RPM respectively. For the coolant, the flow rates,  $3.15 \times 10^{-5} \text{ m}^3/\text{s}$  and  $1.90 \times 10^{-5} \text{ m}^3/\text{s}$  correspond to 100% of pumping capacity and 60% pumping capacity respectively.

	<u>Coolant Flow Rate</u>	<u>Exhaust Flow Rate</u>		
		$0.0118 \text{ m}^3/\text{s}$	$0.0095 \text{ m}^3/\text{s}$	$0.0047 \text{ m}^3/\text{s}$
<u>Coolant Flow Rate</u> (Temperature: $80 \text{ }^\circ\text{C}$ )	$3.15 \times 10^{-5} \text{ m}^3/\text{s}$	N/A	Exhaust Temp: $400 \text{ }^\circ\text{C}$	Exhaust Temp: $400 \text{ }^\circ\text{C}$
	$1.90 \times 10^{-5} \text{ m}^3/\text{s}$	N/A	Exhaust Temp: $400 \text{ }^\circ\text{C}$	Exhaust Temp: $400 \text{ }^\circ\text{C}$
	$3.15 \times 10^{-5} \text{ m}^3/\text{s}$	Exhaust Temp: $300 \text{ }^\circ\text{C}$	Exhaust Temp: $300 \text{ }^\circ\text{C}$	Exhaust Temp: $300 \text{ }^\circ\text{C}$
	$1.90 \times 10^{-5} \text{ m}^3/\text{s}$	Exhaust Temp: $300 \text{ }^\circ\text{C}$	Exhaust Temp: $300 \text{ }^\circ\text{C}$	Exhaust Temp: $300 \text{ }^\circ\text{C}$
	$3.15 \times 10^{-5} \text{ m}^3/\text{s}$	Exhaust Temp: $200 \text{ }^\circ\text{C}$	Exhaust Temp: $200 \text{ }^\circ\text{C}$	Exhaust Temp: $200 \text{ }^\circ\text{C}$
	$1.90 \times 10^{-5} \text{ m}^3/\text{s}$	Exhaust Temp: $200 \text{ }^\circ\text{C}$	Exhaust Temp: $200 \text{ }^\circ\text{C}$	Exhaust Temp: $200 \text{ }^\circ\text{C}$

**Table 2: Test matrix for the experiments. All cases are carried out for two separate coolant flow and exhaust flow geometries.**

## Methodology

The experimental rig is designed to simulate the exhaust and coolant loops of the system. The exhaust gases are simulated using compressed air. The air flow rate is then measured through a rotameter placed in-line with the piping. The air is then passed through an inline heater that is rated for 8 kW at 240 V to achieve the required maximum temperature of 400 °C. Additional tape heaters are used at higher flow rates to ensure the correct temperatures. The air then moves through the test section, with measurement points in the piping to obtain temperature and pressure conditions before and after the test section. These measurements are used ensure correct boundary conditions for the experiment and also for checking the overall pressure drop through the test section.

Water is used in the coolant loop at 80 °C at the two flow rates. It is stored in a reservoir equipped with an immersion heater and circulated in a closed loop through a turbine flow. There are two types of measurements that are made for both the hot and the cold side loops - pressure drop and temperature from either side of the test sections. Figure 38 and Figure 39 show the ports used to measure the pressure drop across the two sections.

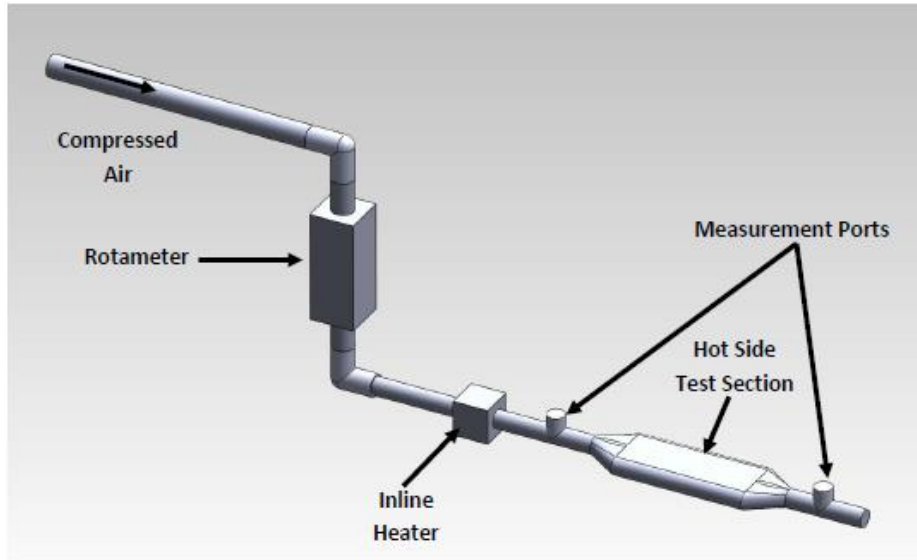


**Figure 38: Schematic of the hot loop.**

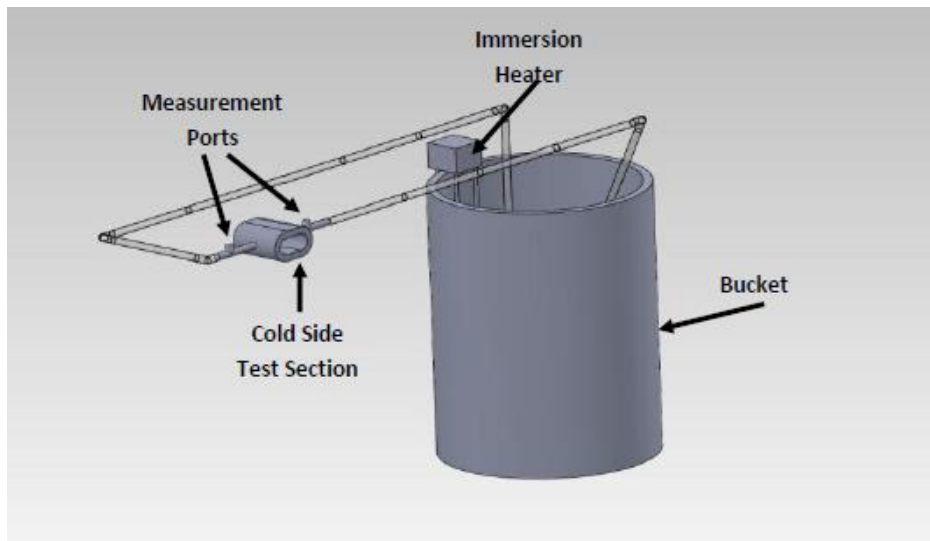


**Figure 39: Schematic of the cold loop.**

In order to ensure that the temperatures do not damage the instrument for the hot side, the tubes from the ports to the manometer are connected using a ball valve. Measurements are taken before the heater for the hot side is started. The thermoelectric generator modules are sandwiched

between the hot and cold sections with a compression fit enforcing maximum contact between all surfaces. Thermocouples are placed between the module and the hot and cold side as shown in Figure 40. Overall, there are four thermocouples placed on each side of the module. This placement allows for measurement of temperature gradients in both spanwise and streamwise direction.

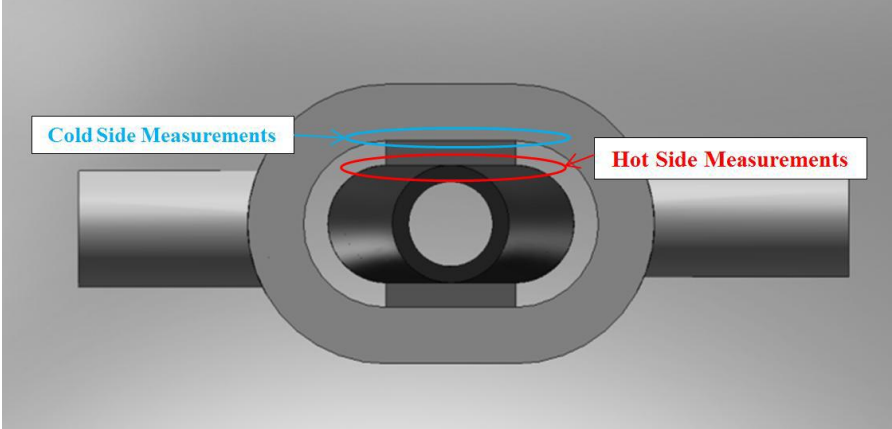


Figure 40: Figure illustrating location of thermocouples for temperature measurement.

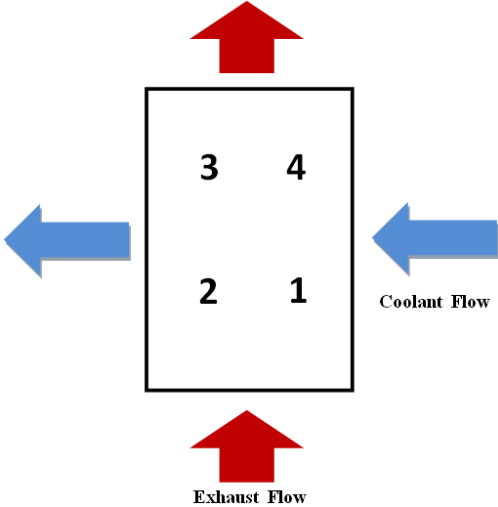


Figure 41: Numbering of thermocouples on the TEG.

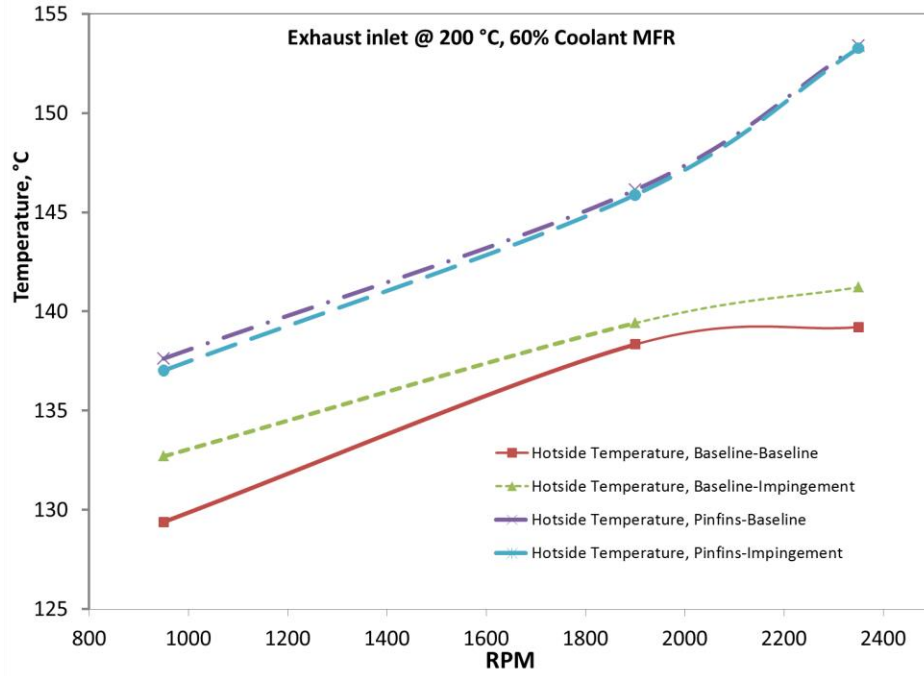
At the beginning of each experiment, water and air flow rates are set to the desired level. Water is heated to 80 °C and the air temperature is set according to the test matrix. Once all conditions reach desirable points, the system is allowed to reach steady state which is monitored by examining temperatures on the TEG module. Once steady state is reached, the temperatures and pressures are recorded and system is allowed to cool down before continuing with the next case.

## **Results & Discussion**

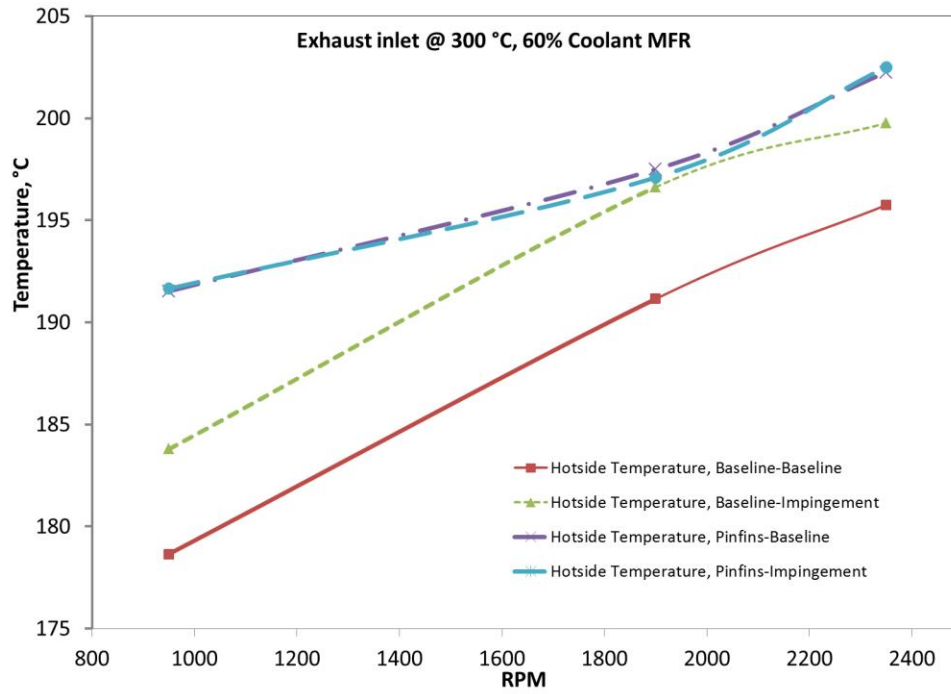
The data from the experiments is processed to provide a map of predicted efficiency based on engine RPM. The TEG module is assumed to be a typical commercial generator made of Bismuth Telluride ( $\text{Bi}_2\text{Te}_3$ ). Equation 2 is used to calculate the efficiency of the thermoelectric generator. The thermocouples are numbered according to their locations as shown in 11. The temperature data in this section is obtained from averaging the temperature recorded by the four thermocouples shown in Figure 41.

There are four combinations of geometry that are examined. As a convention, the first descriptive is for the hot side geometry and the second is for the cold side geometry. Thus, the four cases are baseline-baseline, baseline-impingement, pin-fins-baseline and pin-fins-impingement. We will attempt to demonstrate the improvement in performance of the system with several metrics, most importantly temperatures.

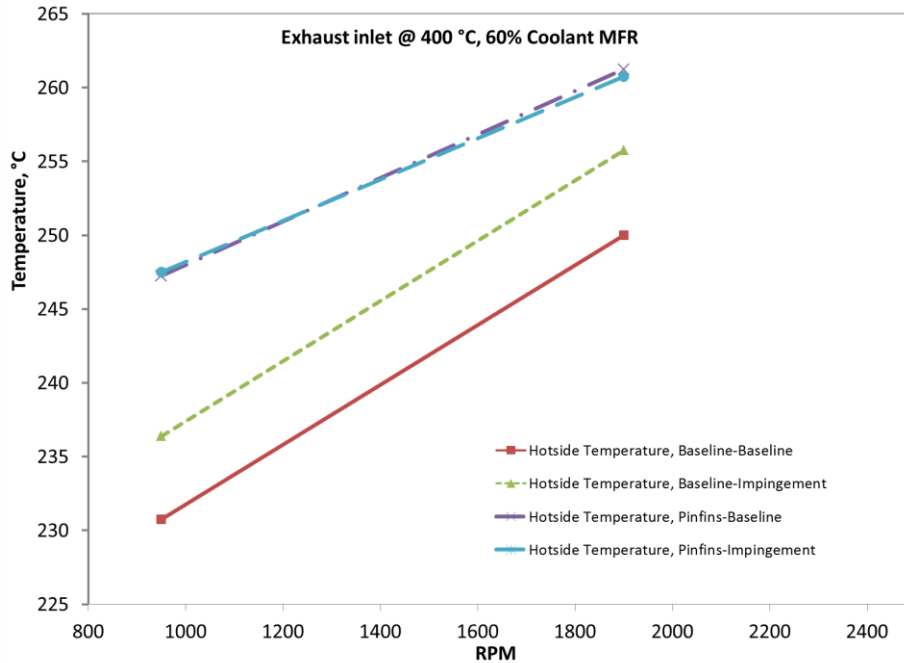
Figure 42a, Figure 42b and Figure 42c, illustrate the effect of varying engine RPM on hot side temperatures with varying exhaust inlet temperatures and different geometry combinations.



a)



b)

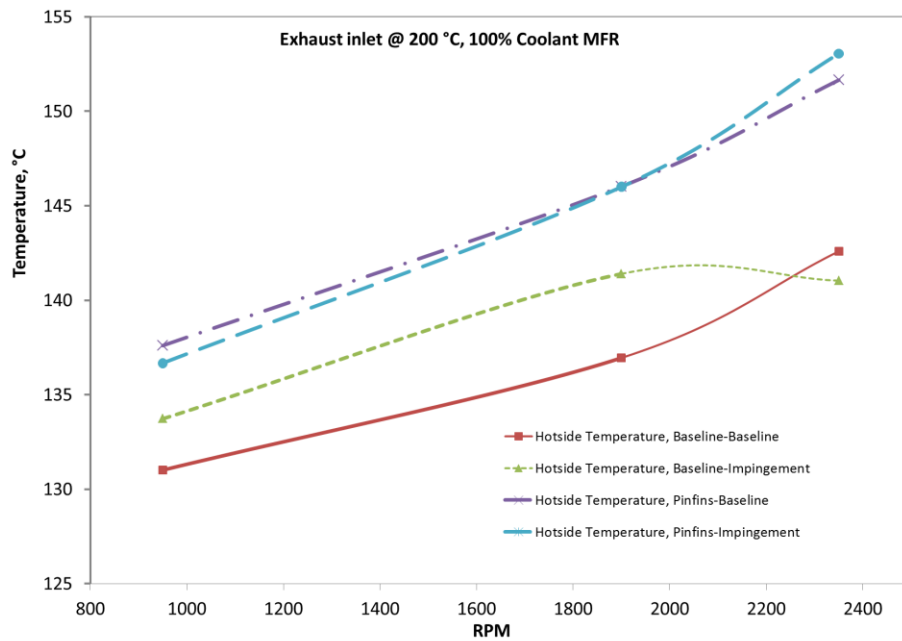


c)

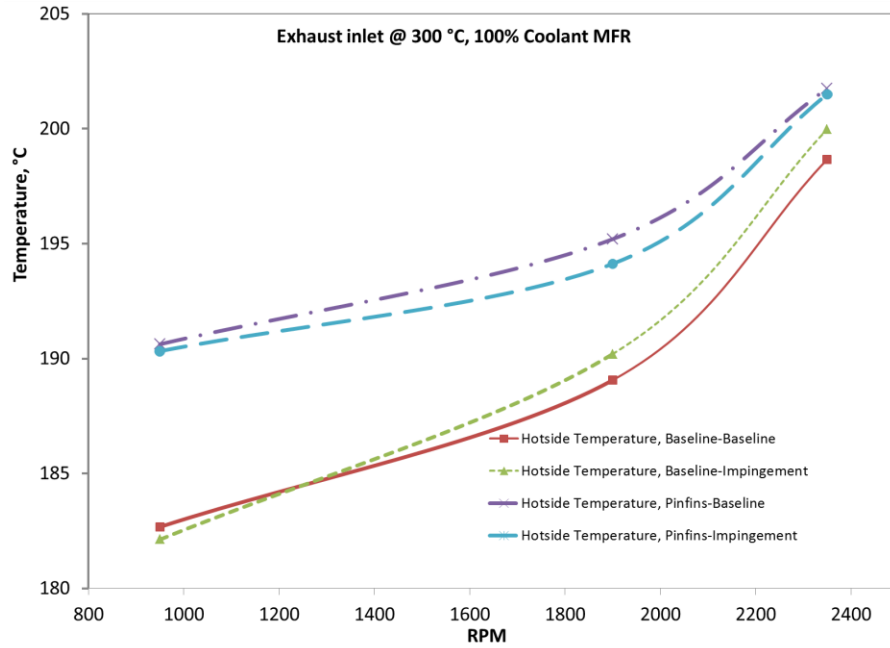
**Figure 42: Variation in hotside temperature with varying engine RPM. Three different hot side inlet temperatures are examined at a fixed coolant mass flow rate capacity of 60%.**

Figure 42a illustrates the change in hot side temperature at an inlet temperature of 200 °C for the four geometry combinations. As is expected, with increasing engine RPM (increased exhaust mass flow rate) the hot side temperature also increases. The figure also shows an increase in hot side temperature going from baseline-baseline to baseline-impingement. The reason for this increase in temperature is that the impingement geometry on the cold side improves heat exchange between coolant and cold surface. This in turn increases the heat being drawn from the exhaust gases. The two cases with pin-fins on the hot side have significantly higher hot side temperatures as versus the baseline hot side cases but do not show a tremendous variation within themselves. The pin-fins are more effective at lower RPMs. This can be explained by the inherently higher turbulence that is present in the case of flows corresponding to higher RPMs as

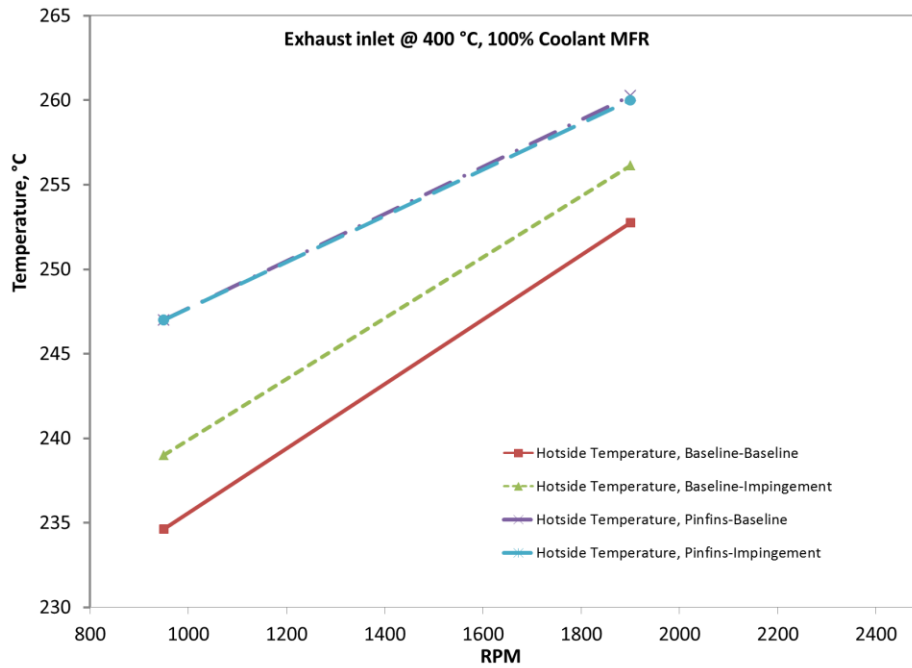
the addition of pin-fins contributes comparatively little to the mixing of the flow. The primary mechanism of increased heat transfer is the increase in surface area. The same trends are also reported in detailed pin-fin studies found in literature [35], [36]. This behavior justifies the application of pin-fins as heat transfer augmentation features in this system as the engine RPM varies considerably with road and driving conditions. These trends are repeated in Figure 42b and Figure 42c and again in Figure 43a, Figure 43b and Figure 43c, which examine the same cases but at a higher coolant pumping capacity (100%).



a)



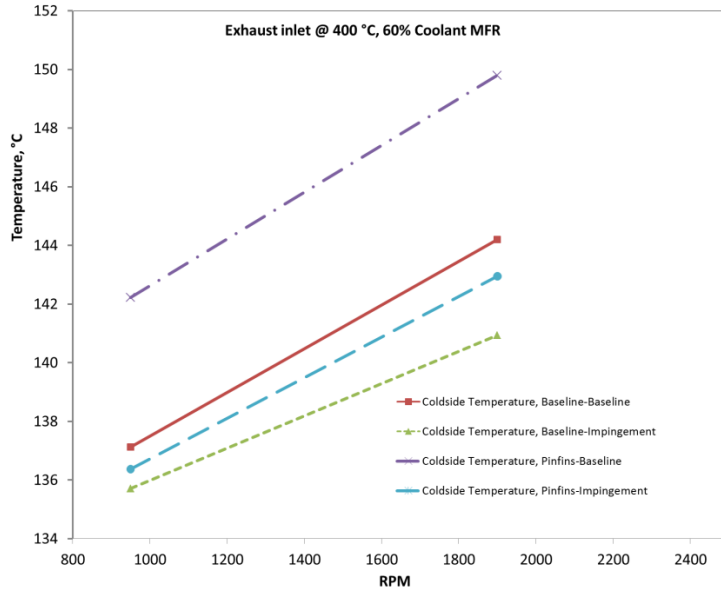
b)



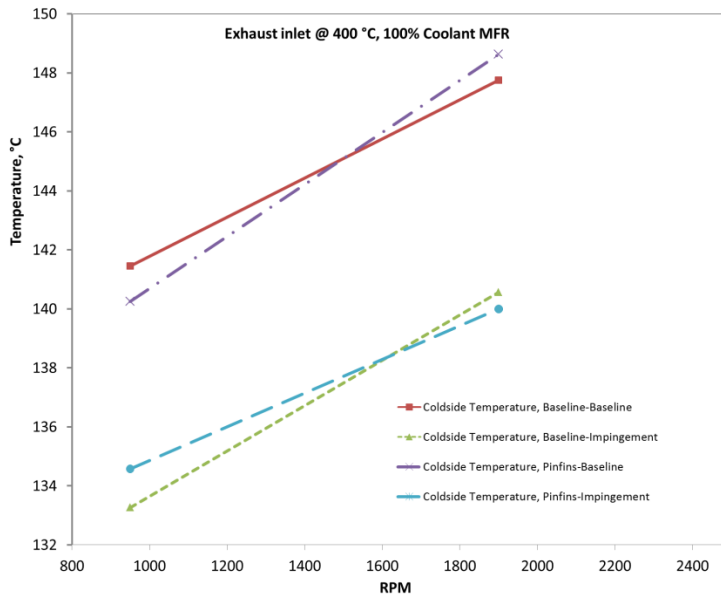
c)

**Figure 43: Variation in hot side temperature with varying engine RPM. Three different hot side inlet temperatures are examined at a fixed coolant mass flow rate capacity of 100%.**

Next, we examine similar trends for the cold side temperatures. The variation in cold side temperatures for lower hot side inlet temperatures is very narrow and within the uncertainty range (98-103 °C) and hence these graphs are not reported. Figure 43a and Figure 43b show the cold side variation in temperature for an exhaust gas inlet temperature of 400 °C and coolant MFR capacity of 60% and 100% respectively. Figure 43a clearly highlights the effect of each of the geometry combinations with the given flow conditions. At the lower coolant mass flow rate, the cooling is strongly dependent on the cold side heat transfer features. The lowest cold side temperatures are achieved when the pin-fins are absent from the hot side and impingement is present on the coolant side. The cold side gets the hottest for the opposite case, i.e. when the coolant side has no cooling features and there are pin-fins on the exhaust gas side. This clearly demonstrates the increased heat flux that is transferred from the exhaust gas to the coolant by the use of the pin-fins on the exhaust side, resulting in hotter temperatures on the cold side as well. It is important to consider the benefits of the increased hot side temperatures against the detrimental effects of hotter cold side temperatures before making a design choice about the implementation of pin-fins on the hot side. The efficacy of the impingement cooling on the cold side is clearly demonstrated by this graph and a strong case for its implementation can be made from this data. The temperatures in the other two cases are very close to each other and thus it is difficult to distinguish between the effects of these two combinations.



a)



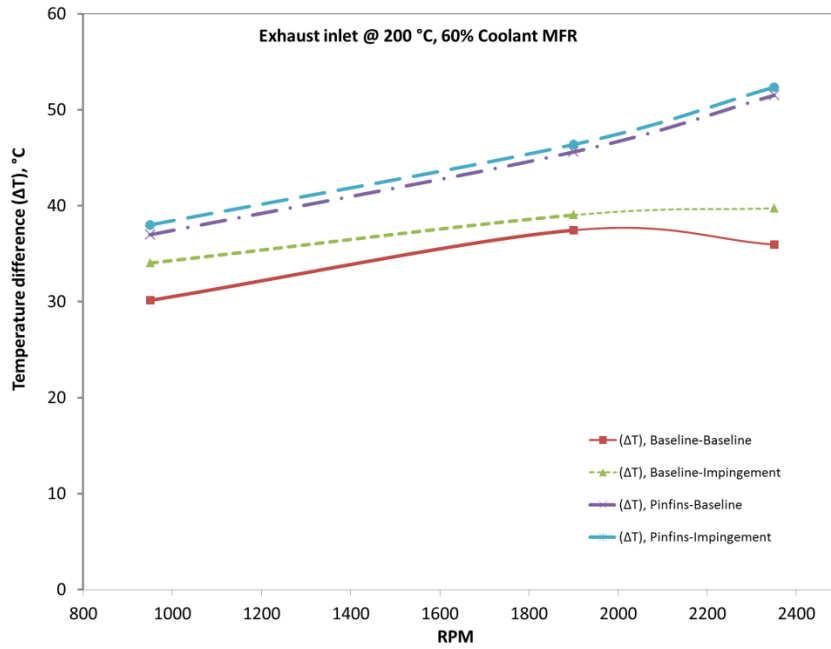
b)

**Figure 44: Variation in cold side temperature with varying engine RPM. An exhaust gas inlet temperature of 400 ° C is examined at coolant mass flow rate capacities of 60% and 100%.**

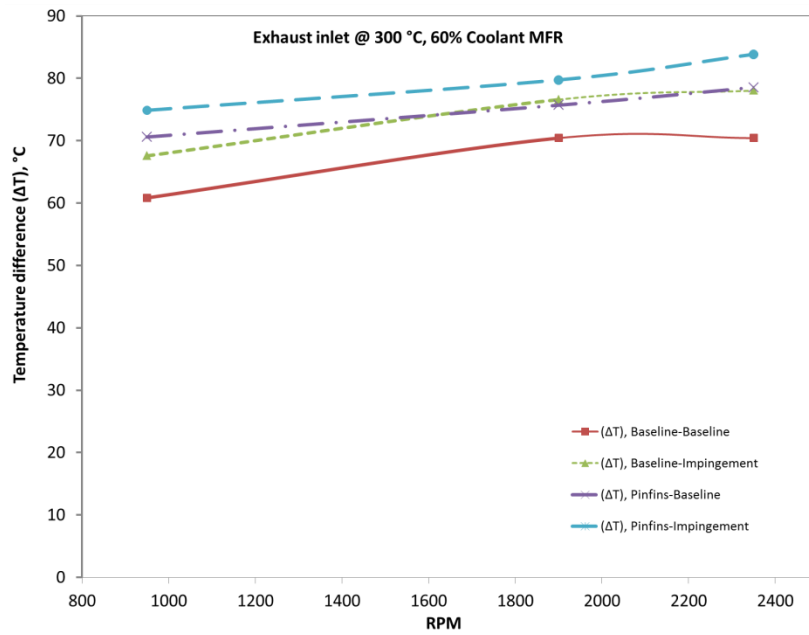
The difference between the hot side and cold side temperatures is equally important as their individual temperatures. This data helps not only to calculate the system efficiency and the generated power, but also guides our design choices on the implementation of heat transfer augmentation techniques on one, or both sides of the system. Figure 45 and Figure 46 show the difference between hot and cold side temperatures for 60% and 100% coolant MFR capacity. The individual subcases follow the same pattern as in Figures Figure 42 and Figure 43. Previously examined data has shown that the cold side temperatures and the hot side temperatures react differently to the various geometry combinations. However the difference between these,  $\Delta T$ , is a bigger factor in determining the overall performance of the thermoelectric generator system. As seen in Figure 45a,  $\Delta T$  is least when there is no heat transfer enhancement on either the hot or cold side of the system. The trends clearly demonstrate that it is in fact beneficial for the  $\Delta T$  to implement pin-fins on the hot side of the system, notwithstanding the hotter cold side temperatures it produces. Implementation of an impinging coolant results in a further increase in  $\Delta T$ . Therefore, the implementation of impingement on the cold side is also justified from this data. This data is extremely valuable in that it clearly advocates one design choice over the others.

In Figure 45b and Figure 45c, similar trends can be seen except that the baseline-impingement and pin-fin baseline cases behave in a different manner. In Figure 45b, these two cases are not significantly different. Figure 45c however suggests a crossover point for engine RPM where one geometry combination is better than the other. It can be inferred that at high exhaust gas inlet temperatures and high engine RPMs, the impingement of the coolant contributes more to the temperature difference than the pin-fins on the exhaust side. This conclusion concurs with our previous deduction that pin-fins are more beneficial at lower RPMs and thus Reynolds numbers.

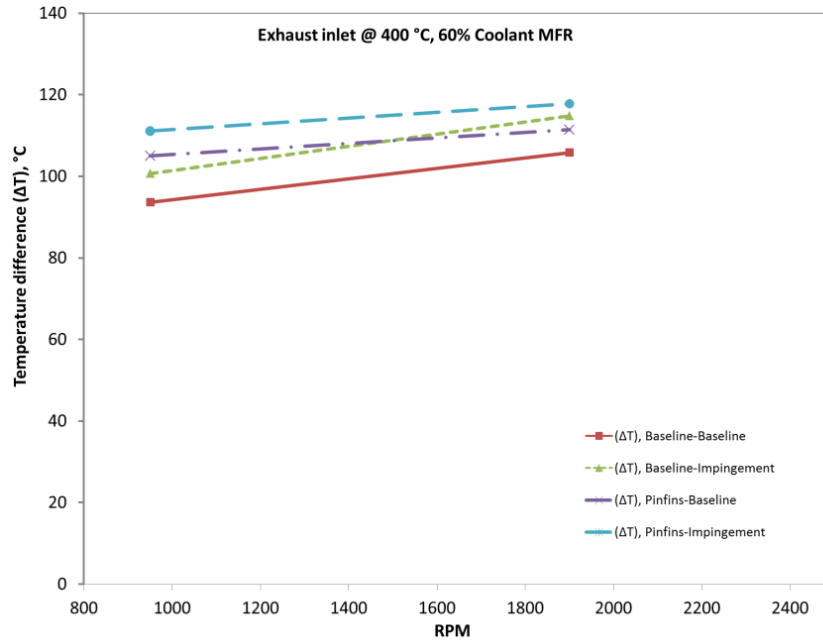
Very similar trends can be observed in Figure 46a as well which shows data at the higher coolant MFR capacity (100%). The temperature data recorded for all cases is shown in Tables 3-6.



a)

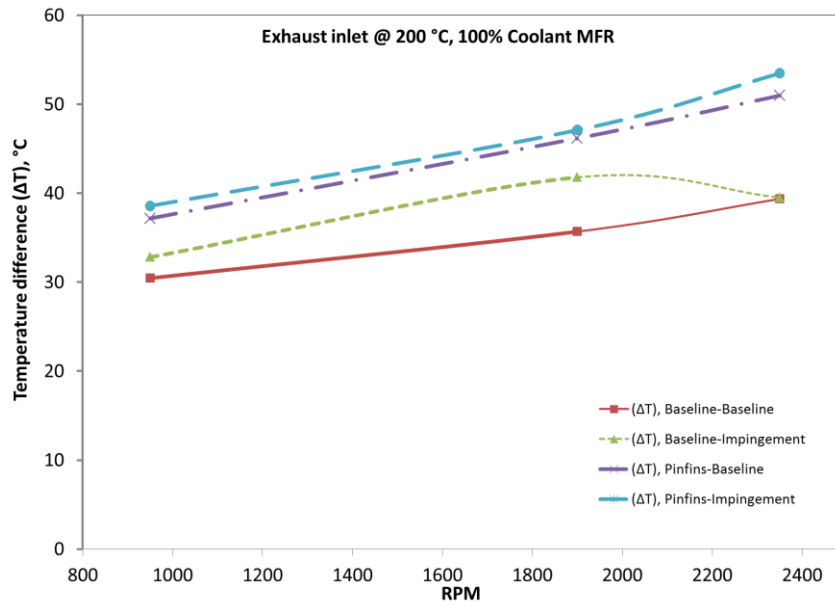


b)

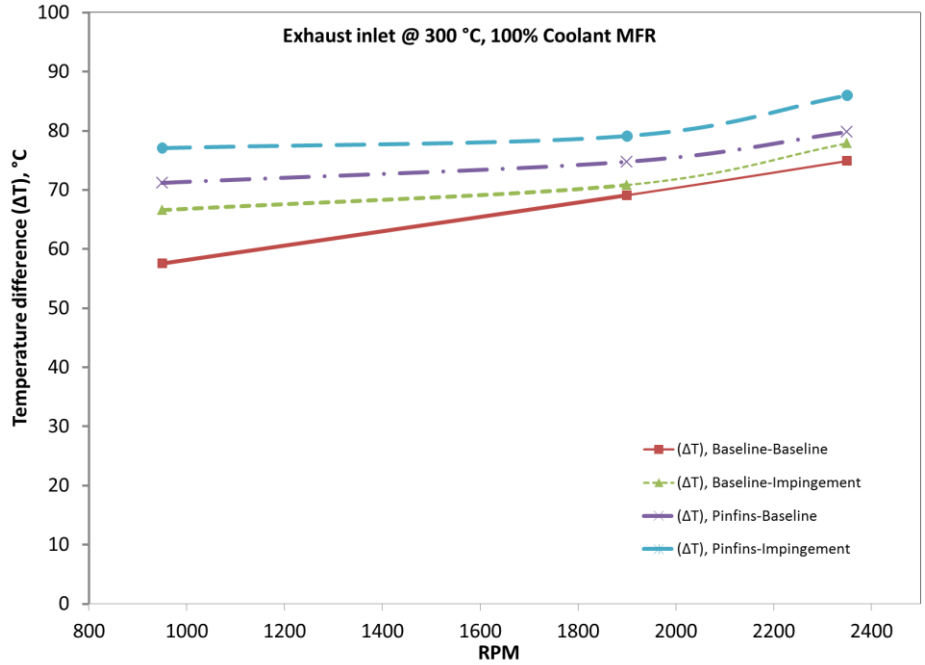


c)

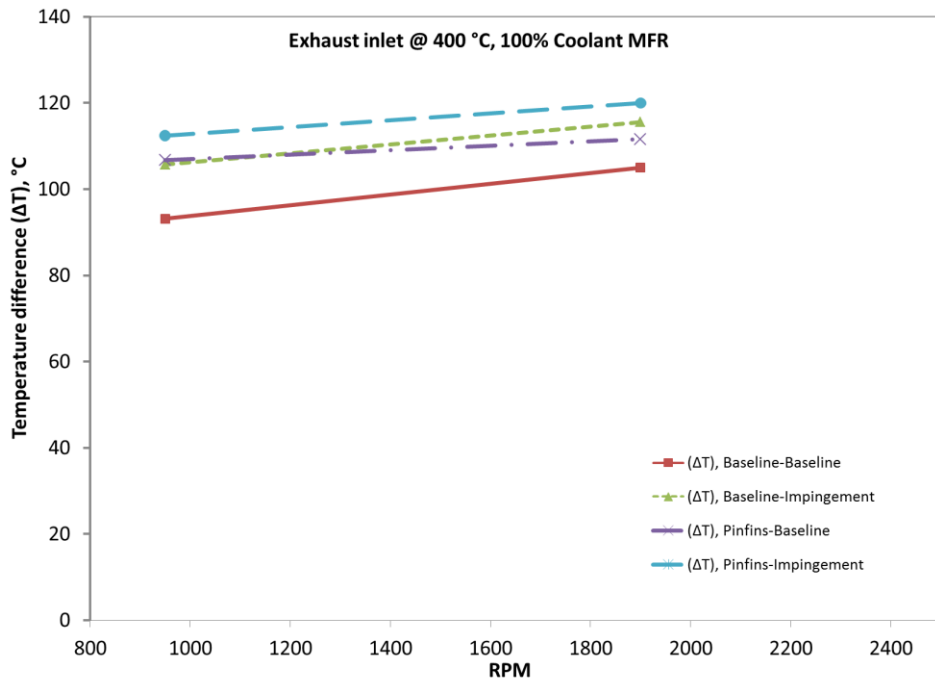
**Figure 45: Variation in  $\Delta T$  with varying engine RPM. Three different hot side inlet temperatures are examined at a fixed coolant mass flow rate capacity of 60%.**



a)



b)



c)

**Figure 46: Variation in  $\Delta T$  with varying engine RPM. Three different hot side inlet temperatures are examined at a fixed coolant mass flow rate capacity of 100%.**

<b><u>Hot Side temperatures, (°C)</u></b>						
<b><i>RPM</i></b>	<b><i>200 °C Inlet, 60% Coolant</i></b>	<b><i>300 °C Inlet, 60% Coolant</i></b>	<b><i>400 °C Inlet, 60% Coolant</i></b>	<b><i>200 °C Inlet, 100% Coolant</i></b>	<b><i>300 °C Inlet, 100% Coolant</i></b>	<b><i>400 °C Inlet, 100% Coolant</i></b>
950	129.3875	178.65	230.75	131.0125	182.675	234.625
1900	138.3375	191.15	250	136.95	189.0625	252.75
2350	139.2125	195.75	N/A	142.5875	198.6625	N/A
<b><u>Cold Side temperatures, (°C)</u></b>						
950	99.25	117.8125	137.125	100.5625	125.1125	141.45
1900	100.8875	120.725	144.2	101.2625	119.95	147.75
2350	103.2625	125.325	N/A	103.225	123.775	N/A
<b><u>ΔT, (°C)</u></b>						
950	30.1375	60.8375	93.625	30.45	57.5625	93.175
1900	37.45	70.425	105.8	35.6875	69.1125	105
2350	35.95	70.425	N/A!	39.3625	74.8875	N/A!

**Table 3: Temperature data for Baseline-Baseline case**

<b><u>Hot Side temperatures, (°C)</u></b>						
<b><i>RPM</i></b>	<b><i>200 °C Inlet, 60% Coolant</i></b>	<b><i>300 °C Inlet, 60% Coolant</i></b>	<b><i>400 °C Inlet, 60% Coolant</i></b>	<b><i>200 °C Inlet, 100% Coolant</i></b>	<b><i>300 °C Inlet, 100% Coolant</i></b>	<b><i>400 °C Inlet, 100% Coolant</i></b>
950	132.7	183.7875	236.375	133.725	182.125	239
1900	139.4125	196.625	255.75	141.4	200.8875	256.125
2350	141.225	199.7625	N/A	141.0375	199.975	N/A
<b><u>Cold Side temperatures, (°C)</u></b>						
950	98.675	116.2125	135.7125	100.9125	115.525	133.2625
1900	100.3875	120.0375	140.9375	99.6125	119.3625	140.5625
2350	101.4875	121.725	N/A	101.5125	122.1	N/A
<b><u>ΔT, (°C)</u></b>						
950	34.025	67.575	100.6625	32.8125	66.6	105.7375
1900	39.025	76.5875	114.8125	41.7875	81.525	115.5625
2350	39.7375	78.0375	N/A	39.525	77.875	N/A

**Table 4: Temperature data for Baseline-Impingement case**

It is important to understand how the temperatures examined thus far affect the overall system performance. Since power is a function of the overall surface area, it cannot be used as a metric of performance for a small scale test rig and efficiency is used instead. Figure 47 shows the improvement in efficiency of the thermoelectric generator due to the enhanced heat transfer in the various geometry combinations. The efficiency is calculated using equation 2.

<b><i>Hot Side temperatures, (°C)</i></b>						
<i>RPM</i>	<i>200 °C Inlet, 60% Coolant</i>	<i>300 °C Inlet, 60% Coolant</i>	<i>400 °C Inlet, 60% Coolant</i>	<i>200 °C Inlet, 100% Coolant</i>	<i>300 °C Inlet, 100% Coolant</i>	<i>400 °C Inlet, 100% Coolant</i>
950	137.625	191.525	247.25	137.6	190.625	247
1900	146.125	194.75	261.25	146.025	195.2	260.25
2350	153.4	202.25	N/A	151.65	201.75	N/A
<b><i>Cold Side temperatures, (°C)</i></b>						
950	100.65	120.925	142.225	100.425	119.425	140.25
1900	100.525	121.8	149.8	99.85	120.425	148.625
2350	101.9	123.7	N/A	100.675	121.95	N/A
<b><i>ΔT, (°C)</i></b>						
950	36.975	70.6	105.025	37.175	71.2	106.75
1900	45.6	72.95	111.45	46.175	74.775	111.625
2350	51.5	78.55	N/A	50.975	79.8	N/A

**Table 5: Temperature data for Pin-fins-Baseline case**

<b><i>Hot Side temperatures, (°C)</i></b>						
<i>RPM</i>	<i>200 °C Inlet, 60% Coolant</i>	<i>300 °C Inlet, 60% Coolant</i>	<i>400 °C Inlet, 60% Coolant</i>	<i>200 °C Inlet, 100% Coolant</i>	<i>300 °C Inlet, 100% Coolant</i>	<i>400 °C Inlet, 100% Coolant</i>
950	137.025	191.65	247.5	136.675	190.325	247
1900	145.875	194.2	260.75	146	194.125	260
2350	153.275	202.5	N/A	153.05	201.5	N/A
<b><i>Cold Side temperatures, (°C)</i></b>						
950	99.025	116.775	136.375	98.1	113.25	134.575
1900	99.5	117.35	142.95	98.9	115	140
2350	100.925	118.65	N/A	99.575	115.525	N/A
<b><i>ΔT, (°C)</i></b>						
950	38	74.875	111.125	38.575	77.075	112.425
1900	46.375	76.85	117.8	47.1	79.125	120
2350	52.35	83.85	N/A	53.475	85.975	N/A

**Table 6: Temperature data for Pin-fins-Impingement case**

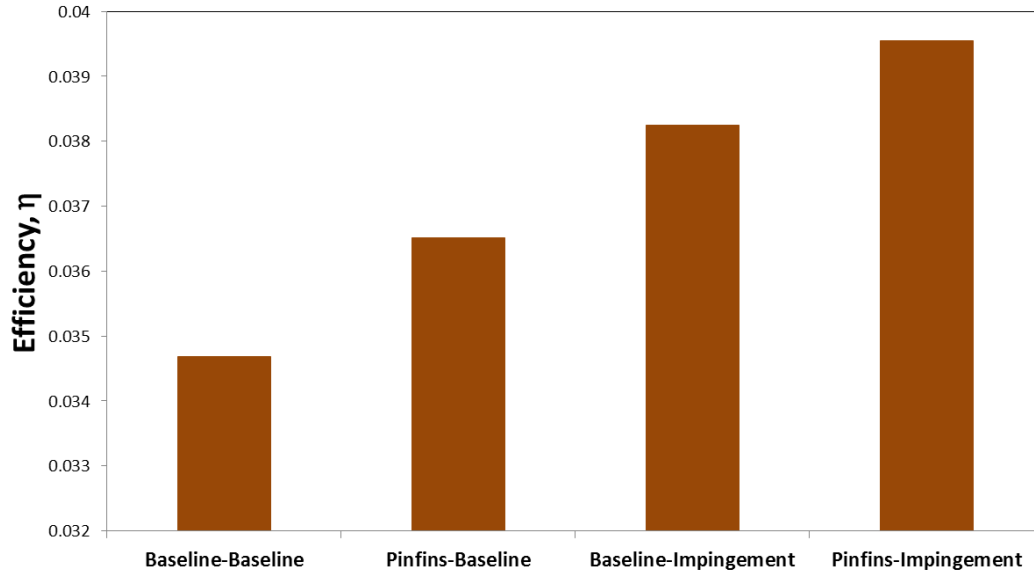


**Figure 47: Increase in efficiency of the TEG with varying geometry combinations. (Exhaust gas inlet@ 400°C, 1900 RPM, 100% coolant MFR capacity)**

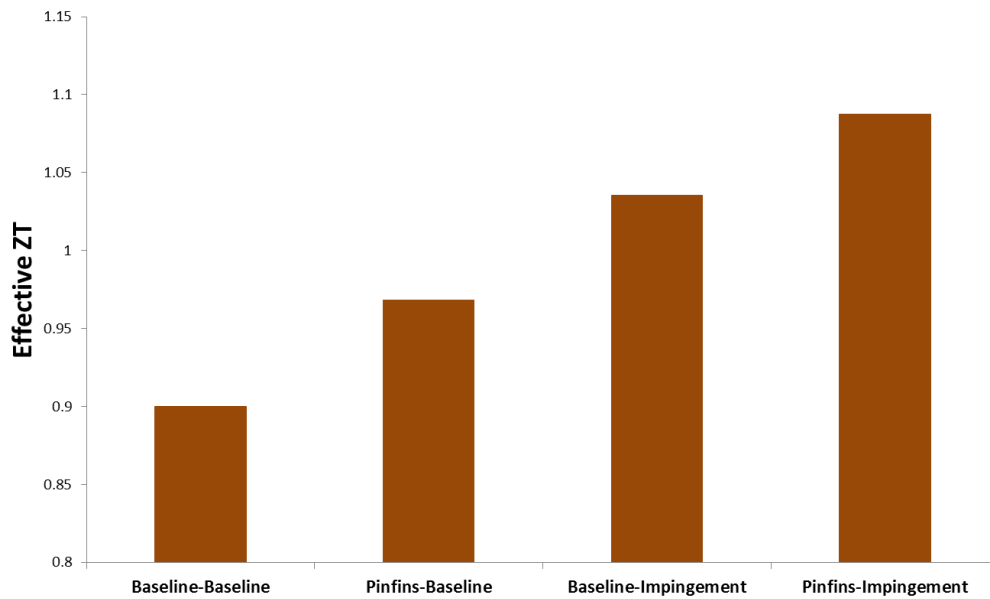


**Figure 48: Effective increase in ZT required to achieve same gain in efficiency for various cases.**

This representative efficiency in Figure 47 case clearly demonstrates the drastic improvement in efficiency that can be achieved by implementing heat transfer enhancement techniques between the TEG and the working fluids. To put this in perspective, Figure 48 shows equivalent increase in  $ZT$  that would be required to achieve the same increase in efficiency. In this case, the temperatures are assumed to be that of the baseline-baseline case and the  $Z$  is assumed to be varying to attain the increase in efficiency seen in Figure 47.

## **Conclusion**

It is clear from the examined data that there are clear and significant advantages to focus on heat transfer augmentation in a thermoelectric generator in addition to improvements in material properties. A viable design for such a thermoelectric generator has been presented, manufactured and tested in this study. Various combinations of geometries, with and without heat transfer augmentation features, have been tested at a variety of flow conditions and detailed results have been provided.

**Chapter 5: An Analysis of effect of contact conductance on system performance efficiency and power generation.**

## AN ANALYSIS OF EFFECT OF CONTACT CONDUCTANCE ON SYSTEM

The previous chapters have detailed the heat transfer enhancement techniques that are proposed for implementation in a waste heat recovery system for automobile exhaust gases. Advanced heat transfer techniques have been examined in order to maximize the temperature gradient across the thermoelectric device by improving heat transfer to and from the source and sink. This study explores the effect of contact conductance between the thermoelectric module and the hot and cold side heat exchangers. A theoretical and numerical analysis is done to determine the importance of contact conductance on the overall efficiency of the system.

### Theory

Since the thermoelectric material has a non-zero thermal conductivity (finite thermal resistance), it cannot allow an arbitrarily large heat flux across it without loss in temperature. Figure 49 shows a thermal model of a thermoelectric energy harvester.  $\Delta T_{\text{supply}}$  is the temperature difference between the heat source and sink.  $\Theta_{\text{TE}}$  is the thermal resistance of the thermoelectric and  $\Theta_{\text{HX}}$  is the combined thermal resistance of the hot and cold side heat exchangers in series with the thermoelectric. The equation governing the heat flux through this system is given as,

$$\Delta T_{\text{HX}} = Q \Theta_{\text{HX}} \quad \text{Equation 6}$$

If all the available temperature difference is across the thermoelectric with no  $\Delta T$  across the heat exchangers, there will be no heat flux ( $Q$ ) through the system as it is in series and no power will be produced. If we assume a fixed  $\Delta T_{\text{supply}}$  (known from source and sink temperatures) and increase  $\Delta T_{\text{HX}}$ ,  $\Delta T_{\text{TE}}$  will reduce ( $\Delta T_{\text{TE}} = \Delta T_{\text{supply}} - \Delta T_{\text{HX}}$ ), thus reducing efficiency. According

to this, an optimum thermal resistance can be calculated which will allow for the maximum power output through the system.

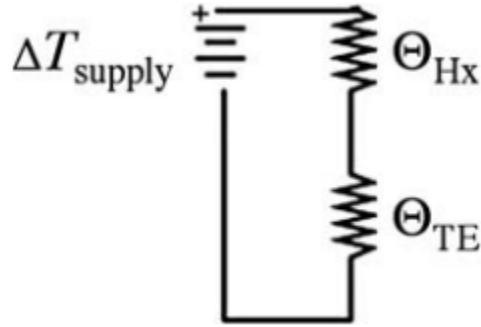


**Figure 49. Typical thermal circuit in a thermoelectric energy harvesting device**

From the thermal circuit in Figure 49, we can show:

$$\Delta T_{TE} = \Delta T_{supply} \cdot \frac{\Theta_{TE}}{\Theta_{HX} + \Theta_{TE}} \quad \text{Equation 7}$$

the heat flow through the circuit is given by:

$$Q = \frac{\Delta T_{supply}}{\Theta_{HX} + \Theta_{TE}} \quad \text{Equation 8}$$

It can be shown from equation 2 that efficiency is directly proportional to the temperature difference across the TEG. Therefore power is given by,

$$P = \eta \cdot \Delta T_{supply}^2 \cdot \frac{\Theta_{TE}}{(\Theta_{HX} + \Theta_{TE})^2} \quad \text{Equation 9}$$

From Equation 9, maximum power is achieved when  $\Theta_{HX}$  is equal to  $\Theta_{TE}$ . When this happens, the temperature difference across the TEG,  $\Delta T_{TE}$ , is exactly half of the available temperature difference,  $\Delta T_{supply}$ .

The thermal resistance of the thermoelectric,  $\Theta_{TE}$ , comprises of several different parts. It accounts for the thermal resistance of the thermoelectric material's n and p type legs, the thermal contact resistance between the legs and the junction materials, the thermal resistance of the junction materials themselves and finally the thermal contact resistance between the junction material and the heat exchangers. In the case of a commercially bought TEG module, the first three components are fixed and cannot be controlled. With the help of numerical simulations, Ziolkowski et al have shown the contact resistances between the thermoelectric material and the junction bridges to be negligible [37] The thermal contact resistance between the TEG module and the heat exchanger however is a function of the system design and assembly and thus can be modified with the use of various techniques like, thermal grease, contact pressure, surface finish etc.

Several studies have attempted to understand the effects of thermal contact resistances on system performance of thermoelectric generators. Hogblom et al used a combination of numerical simulations and experiments to determine the contact resistances at various junctions in the setup [38]. They determined that simulations consistently over-predicted power output of the TEG by upto 200% and heat flux by approximately 50% and that the efficiency of power output can be increased by minimizing contact resistances. Similar conclusions were drawn by the work of Ebling et al [39]. Both these studies have been done on a small scale thermoelectric module without consideration for the application.

There has been extensive research in the field of thermal contact resistance and it is typically reported to be in the range of 0.000005 to 0.0005 m<sup>2</sup>K/W depending upon the specific material properties of the two surfaces in question [40]. An estimate of the thermal resistances of the TE modules can be done to determine if the contact resistances are significant. If thermal conductivity of the TEG material is  $k_{TEG}$  then the thermal contact resistance can be estimated by the expression,

$$\beta = l/k_{TEG} \quad \text{Equation 10}$$

where  $l$  is the length of the TEG legs. This length is typically of the order of 1mm and the thermal conductivity of the bulk material in a TEG is approximately 2 W/mK [38]. This results in a thermal contact resistance of approximately 0.0005 m<sup>2</sup>K/W. This analysis shows that for certain interfaces where the contact resistance is of the order of 10<sup>-4</sup> and greater, it is comparable to the overall bulk contact resistance and should be taken into account while predicting system performance.

This analysis provides a starting point for steps that can be taken to understand and quantify the power output of the final system. This study attempts to understand the effects of thermal contact resistance on the overall efficiency of the system by analyzing the temperature distributions that are produced on the hot and cold side of the thermoelectric generator while taking into account the thermal contact resistances between the TEG modules and the heat exchangers. This analysis is done on previously developed heat exchanger designs while adding heat transfer enhancement features on the hot and cold side of the heat exchangers [27], [41]. Several different contact resistances are considered and the effects of these are analyzed. The basic heat exchanger design is described in the following sections along with the computational methodology and boundary conditions.

## Methodology

The designs in this study were modeled using commercially available software, ANSYS CFX. The k- $\omega$  model was used for turbulence. The thermoelectric material considered was Bismuth Telluride ( $\text{Bi}_2\text{Te}_3$ ), the thermal properties for which can be seen in Table 1.

## Geometry and Boundary Conditions

The geometry (Figure 3) consists of a pipe containing the exhaust gases expanding into a flattened-oval section in order to slow them down and increase surface area. Vertical pipes pass through the channel in order to enhance conduction, create turbulence and promote mixing in the exhaust gases. The representative TEG geometries (material- $\text{Bi}_2\text{Te}_3$ ) are attached to the flat surfaces of the oval sections. A channel containing the coolant flowing in a direction perpendicular to the exhaust gases is wrapped around this section.

The exhaust gas pipe is considered adiabatic in order to get its temperature to the exhaust gas temperature as might be expected. Similar reasoning applies for the coolant pipe. The exhaust gas inlet velocity is taken to be 20 m/s based on a 2.4 l, v6 engine at 3000 RPM and the cross section of the pipe. The hot side gas temperature at inlet to the heat exchanger is assumed to be 400 °C. For the coolant, the maximum mass flow rate is assumed to be 10 l/min and temperature is 100 °C.[16]

Based on work previously published by this author, the contact conductance study is done with the addition of heat transfer enhancement features namely, pin-fins on the hot side and impinging jets on the cold side. These features have been independently evaluated both experimentally and

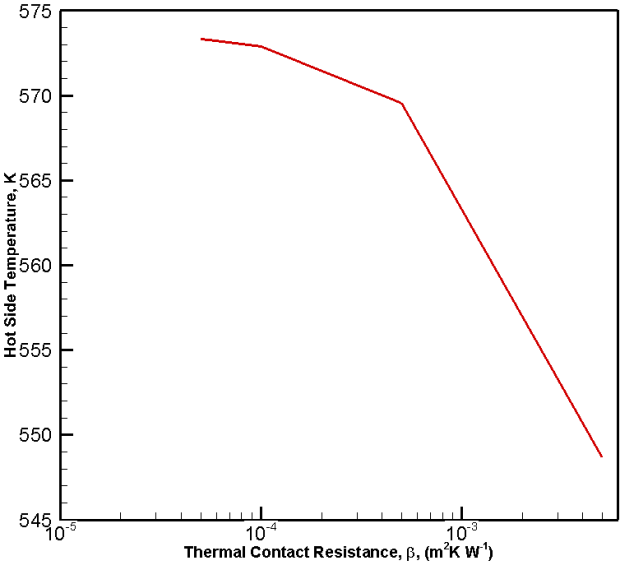
numerically for various parameters like pin fin shape, height, aspect ratio, configuration, hole diameter, hole l/d ratio etc. at the operating conditions in this application [27], [35], [36], [41].

In addition the boundary conditions described above, the simulation are carried out with a range of thermal contact resistances between the interfaces of TEG-Exhaust pipe and TEG-Coolant pipe. The range that is studied is chosen carefully based on maximum and minimum reported values of thermal contact resistance ion literature, while keeping in mind the previous analysis which showed that order of magnitude of the bulk thermal resistance in the TEG is  $5 \times 10^{-4} \text{ m}^2\text{K/W}$ . There are a total of four values on contact resistance that are studied:  $5 \times 10^{-4} \text{ m}^2\text{K/W}$ ,  $5 \times 10^{-5} \text{ m}^2\text{K/W}$ ,  $1 \times 10^{-4} \text{ m}^2\text{K/W}$  and  $5 \times 10^{-3} \text{ m}^2\text{K/W}$ . The last case is studied to evaluate the unlikely scenario where thermal contact resistances dominate the heat transfer through the system. Values of contact resistances that are in the lower end of the range are ignored as they are more than two orders in magnitude smaller than the bulk thermal resistance. Results from this analysis are shown in the following section.

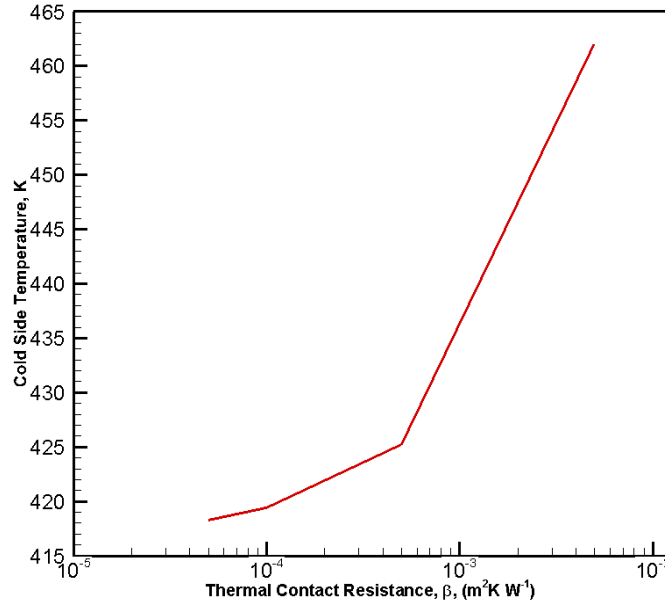
## **Results & Discussion**

Figure 50 and Figure 51 show the area averaged temperature on the hot and cold side respectively. In Figure 50, it can be seen that the hot side temperature drops rapidly with increasing thermal contact resistances. This is expected since the addition thermal resistances reduces the overall heat flux through the system and results in inefficient heat transfer to the representative thermoelectric modules. Similarly, a higher thermal contact resistance between the cold side of the modules and the coolant pipe results in reduced cooling by the working fluid causing higher temperatures on the cold side of the module. This is seen in Figure 51. This

combined effect results in a severe drop in the temperature difference,  $\Delta T$ , between the hot and cold side of the thermoelectric modules. This drop is apparent from Figure 52 which plots these key variables.



**Figure 50: Thermoelectric hot side average temperature variation with thermal contact resistance**



**Figure 51: Thermoelectric cold side average temperature variation with thermal contact resistance**

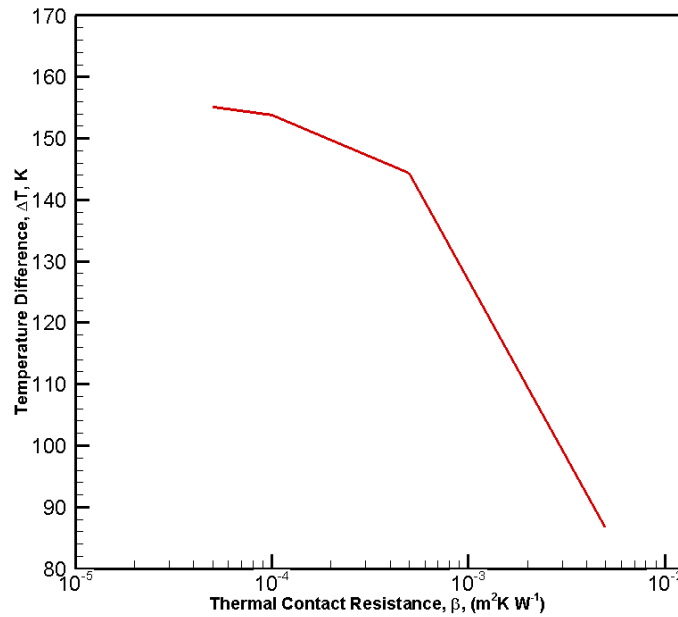


**Figure 52: Average temperature difference between hot and cold side vs. thermal contact resistance**

Equation 2 clearly demonstrates that the efficiency of a TEG depends directly on the thermal gradient across it. Figure 53 uses this equation to plot the change in efficiency of the device due to increasing thermal contact resistance while keeping all other quantities the same. This graph

follows a trend similar to that of Figure 50 and Figure 52. The drop in projected efficiency is gradual in the lower range of thermal contact resistances but is drastically affected when the thermal contact resistance is increased to a large value.

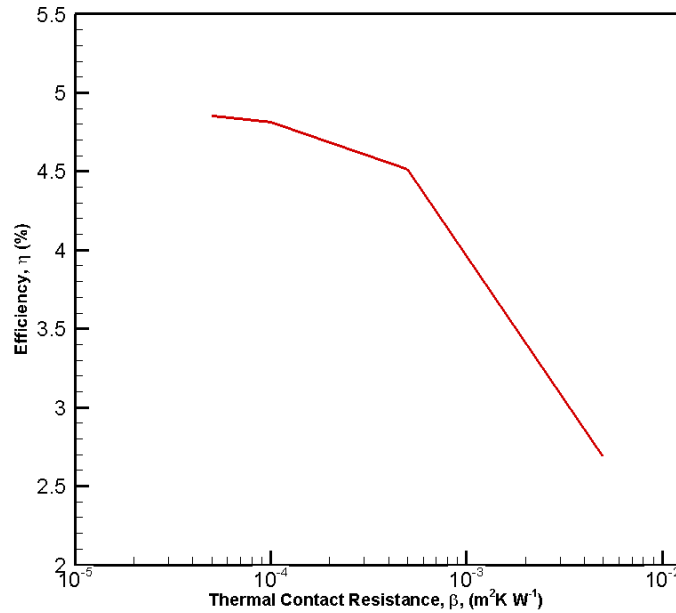


**Figure 53: Projected thermoelectric efficiency vs. thermal contact resistance**

The efficiency of the TEG system drops by as much as 50% in the presence of a high thermal contact resistance between TEG and heat exchanger. It is worth noting that the efficiency is drastically affected only when the thermal contact resistance is extremely high. For cases where the thermal resistance of the bulk material itself dominates the heat transfer, thermal contact resistances affect performance only minimally. It is therefore advisable to perform a tuning analysis on any thermoelectric power generation system to balance the various thermal resistances to result in maximum power output. In order to control the thermal resistance of the

bulk material, the simplest approach is to make the thermoelectric legs longer. In the case of commercially bought TEG modules, the same effect can also be achieved by stacking multiple modules in series (thermally). This method however increases the overall thermal resistance and leads to a lower heat flux through the system resulting in lower power yield.

## **Conclusions**

Thermal contact resistances can have an adverse effect on the system performance of a thermoelectric power generator in terms of both, efficiency and power. It is advisable to ensure proper thermal coupling between the thermoelectric modules and heat exchangers in order to minimize thermal contact resistances. In the presence of a large thermal contact resistance, efficiency of the system can reduce by as much as 44% resulting in drastically reduced power yield.

## CONCLUSIONS

The work discussed in this dissertation provides a comprehensive treatment of a thermoelectric generator's heat exchanger system. The designs developed here facilitate a significant improvement in thermoelectric module performance by increasing the temperature available to the module. All the designs have been modeled with RANS turbulence models with 3 dimensional conjugate heat transfer being examined.

Heat transfer enhancement methods were also evaluated experimentally which could improve the performance of thermoelectric power generators in automotive applications. Valuable data on pin-fin geometry has been made available in the course of this work. The study also evaluated heat transfer enhancement characteristics with varying fin height to channel height ratio while maintaining a constant hydraulic diameter. The pin-fins were examined in a fixed configuration array at pin heights that ranged between 15 % and 50 % of the channel height. The results indicate that diamond shaped pin fins gave the greatest enhancement in heat transfer when compared with other shapes. Data from these experiments show that maximum heat transfer is achieved when the pin fin to channel height ratio is 0.5. These pin-fins are tested at exhaust pipe representative conditions and were determined to be an effective way to enhance heat transfer through the conjugate system.

Experiments were also performed on a small scale system representing the hot and cold side geometries in a thermally coupled environment with the coolant and exhaust loop simulated in a lab environment. Four different combinations of the heat exchanger geometries were considered over a range of engine representative conditions. The data from these experiments matches well

with numerical data and also reaffirms conclusions from the study on pin-fin heat transfer enhancement.

Finally, a study on the effects of contact conductance is performed which shows that a variation in contact conductance has significant effect on the system performance, especially at higher contact resistances. This also paves the path for future work in this area. It is worthwhile to investigate methods of reducing the contact resistance between the thermoelectric module and the heat exchangers or to make the performance insensitive to contact resistance within a reasonable working range. It is also advisable to perform full scale testing on the system by installation of the system in a vehicle. This will further cement the viability of this device as a waste heat recovery method for automobile exhaust gases.

## NOMENCLATURE

$\alpha$	thermal diffusivity of ABS plastic, Seebeck coefficient
$\lambda$	thermal conductivity
$\eta$	TEG efficiency
$\rho$	density
$\sigma$	Electrical Conductivity
$\mu$	dynamic viscosity of working fluid
$D_{h-pf}$	hydraulic diameter of pin fins
$D_{h-ch}$	hydraulic diameter of channel
$h$	pin fin height
$H$	height of channel
$htc$	convective heat transfer coefficient,
$k$	thermal conductivity
$L$	length of channel
$Nu$	Nusselt number
$R$	correlation factor
$Re$	Reynolds number
$RPM$	Revolutions per minute
$S_{sp}$	spanwise spacing (pitch)
$S_{st}$	streamwise spacing (pitch)
$t$	thickness of walls, time
$T$	temperature
$T_i$	initial wall temperature
$T_\infty$	bulk fluid temperature

<b><math>T_h</math></b>	Hot Side Temperature, K
<b><math>T_c</math></b>	Cold Side Temperature, K
<b><math>T_{ms}</math></b>	main stream air temperature
<b><math>T_w</math></b>	wall temperature
<b><math>\Delta T</math></b>	Temperature difference
<b>TEG</b>	Thermoelectric generator
<b><math>u</math></b>	main channel inlet velocity
<b><math>W</math></b>	width of the main channel
<b><math>x</math></b>	x-axis in a rectangular coordinate system
<b><math>Z</math></b>	Figure of merit
<b><math>ZT</math></b>	Dimensionless thermoelectric figure of merit

## REFERENCES

- [1] K. M. Saqr, M. K. Mansour, and M. N. Musa, "Thermal design of automobile exhaust based thermoelectric generators: Objectives and challenges," *Int. J. Automot. Technol.*, vol. 9, no. 2, pp. 155–160, 2008.
- [2] D. M. Rowe, "Thermoelectric waste heat recovery as a renewable energy source," *Int. J. Innov. Energy Syst. Power*, vol. 1, no. 1, pp. 13–23, 2006.
- [3] J. Vázquez, M. A. Sanz-Bobi, R. Palacios, and A. Arenas, "State of the art of thermoelectric generators based on heat recovered from the exhaust gases of automobiles," in *Proc. 7th European Workshop on Thermoelectrics*, 2002, no. 17.
- [4] J. Yang, "Potential applications of thermoelectric waste heat recovery in the automotive industry," in *Thermoelectrics, 2005. ICT 2005. 24th International Conference on*, 2005, pp. 170–174.
- [5] K. Wojciechowski, J. Merkisz, P. Fuć, P. Lijewski, M. Schmidt, and R. Zybała, "Study of Recovery of Waste Heat From the Exhaust of Automotive Engine," *Pozn. Univ. Technol. Poland, e-mail gcwojcie@ cyf-kr. edu. pl*, 2007.
- [6] G. J. Snyder, "Thermoelectric energy harvesting," in *Energy Harvesting Technologies*, Springer, 2009, pp. 325–336.
- [7] K. T. Zorbas, E. Hatzikraniotis, and K. M. Paraskevopoulos, "Power and Efficiency calculation in commercial TEG and application in wasted heat recovery in automobile," in *Proc. of 5th European Conference on Thermoelectrics*, 2007, p. T8.
- [8] M. Chen, S. J. Andreasen, L. Rosendahl, S. K. Kær, and T. Condra, "System modeling and validation of a thermoelectric fluidic power source: Proton Exchange Membrane Fuel Cell and Thermoelectric Generator (PEMFC-TEG)," *J. Electron. Mater.*, vol. 39, no. 9, pp. 1593–1600, 2010.
- [9] D. T. Crane and J. W. LaGrandeur, "Progress report on BSST-Led US department of energy automotive waste heat recovery program," *J. Electron. Mater.*, vol. 39, no. 9, pp. 2142–2148, 2010.
- [10] A. W. Serksnis, "THERMOELECTRIC GENERATOR FOR AN AUTOMOTIVE CHARGING SYSTEM," in *Proceedings of the 11th Intersociety Energy Conversion Engineering Conference, September 12-17, 1976.*, 1976, no. SAE 769274.
- [11] J. C. Bass, R. J. Campana, and N. B. Elsner, "Thermoelectric generator development for heavy-duty truck applications," in *SAE CONFERENCE PROCEEDINGS P*, 1992, p. 743.

- [12] U. Birkholz, E. GroB, U. Stohrer, K. Voss, D. O. Gruden, and W. Wurster, "Conversion of waste exhaust heat in automobiles using FeSi<sub>2</sub> thermoelements," in *Proc. 7th International Conference on Thermoelectric Energy Conversion*, 1988, pp. 124–128.
- [13] K. Ikoma, M. Munekiyo, K. Furuya, M. Kobayashi, T. Izumi, and K. Shinohara, "Thermoelectric module and generator for gasoline engine vehicles," in *Thermoelectrics, 1998. Proceedings ICT 98. XVII International Conference on*, 1998, pp. 464–467.
- [14] N. Espinosa, M. Lazard, L. Aixala, and H. Scherrer, "Modeling a thermoelectric generator applied to diesel automotive heat recovery," *J. Electron. Mater.*, vol. 39, no. 9, pp. 1446–1455, 2010.
- [15] H. Wang, W. D. Porter, and J. Sharp, "Thermal conductivity measurements of bulk thermoelectric materials," in *Thermoelectrics, 2005. ICT 2005. 24th International Conference on*, 2005, pp. 91–94.
- [16] "Advanced Power electronics and electric Machinery Program (FY 2007 Annual Report)," 2007.
- [17] S. V. J. Narumanchi, J. Y. Murthy, and C. H. Amon, "Influence of pulsating submerged liquid jets on chip-level thermal phenomena," *J. Electron. Packag.*, vol. 125, no. 3, pp. 354–361, 2003.
- [18] E. N. Wang, L. Zhang, L. Jiang, J.-M. Koo, J. G. Maveety, E. A. Sanchez, K. E. Goodson, and T. W. Kenny, "Micromachined jets for liquid impingement cooling of VLSI chips," *Microelectromechanical Syst. J.*, vol. 13, no. 5, pp. 833–842, 2004.
- [19] M. Fabbri, S. Jiang, and V. K. Dhir, "Experimental investigation of single-phase micro jets impingement cooling for electronic applications," in *ASME 2003 Heat Transfer Summer Conference*, 2003, pp. 461–468.
- [20] Y. Cheng, A. A. O. Tay, and X. Hong, "An experimental study of liquid jet impingement cooling of electronic components with and without boiling," in *Electronic Materials and Packaging, 2001. EMAP 2001. Advances in*, 2001, pp. 369–375.
- [21] B. R. Hollworth and M. Durbin, "Impingement cooling of electronics," *J. Heat Transfer*, vol. 114, no. 3, pp. 607–613, 1992.
- [22] P. R. Parida, S. V Ekkad, and K. Ngo, "Innovative liquid cooling configurations for high heat flux applications," in *Thermal and Thermomechanical Phenomena in Electronic Systems (ITherm), 2010 12th IEEE Intersociety Conference on*, 2010, pp. 1–8.
- [23] J.-C. Han, S. Dutta, and S. Ekkad, *Gas turbine heat transfer and cooling technology*. Taylor & Francis, 2012.

- [24] M. K. Chyu, S. C. Siw, and H. K. Moon, "Effects of Height-to-Diameter Ratio of Pin Element on Heat Transfer From Staggered Pin-Fin Arrays," 2009.
- [25] J. S. Park, K. M. Kim, D. H. Lee, H. H. Cho, and M. K. Chyu, "Heat Transfer on Rotating Channel With Various Heights of Pin-Fin," 2008.
- [26] S. Siw, M. Chyu, and M. A. Alvin, "Heat Transfer Enhancement of Internal Cooling Passage with Triangular and Semi-Circular Shaped Pin-Fin Arrays," *ASME Pap. No. GT2012-69266*, 2012.
- [27] J. Pandit, M. Dove, S. Ekkad, and S. Huxtable, "Heat Exchanger Design for Waste Heat Recovery from Automobile Exhaust Using Thermoelectric Generators," in *Proc., 50th AIAA Aerospace Sciences Meeting. Nashville, Tennessee*, 2012.
- [28] E. I. Esposito, S. V Ekkad, K. Yong, and P. Dutta, "Novel jet impingement cooling geometry for combustor liner backside cooling," *J. Therm. Sci. Eng. Appl.*, vol. 1, no. 2, 2009.
- [29] E. Esposito and S. V Ekkad, "Jet Impingement Heat Transfer Visualization Using a Steady State Liquid Crystal Method," *J. Heat Transfer*, 2006.
- [30] S. V Ekkad and J.-C. Han, "A transient liquid crystal thermography technique for gas turbine heat transfer measurements," *Meas. Sci. Technol.*, vol. 11, no. 7, p. 957, 2000.
- [31] S. J. Kline and F. A. McClintock, "Describing Uncertainties in Single Sample Experiments," *Mech. Eng. (Am. Soc. Mech. Eng.)*, 75, pp. 3–8, 1953.
- [32] J. A. Lamont, S. V Ekkad, and M. A. Alvin, "Detailed Heat Transfer Measurements Inside Rotating Ribbed Channels Using the Transient Liquid Crystal Technique," *J. Therm. Sci. Eng. Appl.*, vol. 4, p. 11002, 2012.
- [33] P. Jaideep, D. Megan, E. Srinath, and H. Scott, "Heat Exchanger Design for Waste Heat Recovery from Automobile Exhaust Using Thermoelectric Generators," in *50th AIAA Aerospace Sciences Meeting including the New Horizons Forum and Aerospace Exposition*, American Institute of Aeronautics and Astronautics, 2012.
- [34] J. Yang and T. Caillat, "Thermoelectric materials for space and automotive power generation," *MRS Bull.*, vol. 31, no. 03, pp. 224–229, 2006.
- [35] J. Pandit, M. Dove, S. Ekkad, and S. Huxtable, "Effect Of Partial 3-Dimensional Pin Fin Geometry For Heat Transfer Enhancement In High Aspect Ratio Channels," *Proc. IMECE 2012*, 2012.
- [36] J. Pandit, M. Dove, S. V Ekkad, and S. Huxtable, "Effect Of Variation In Channel Height On Heat Transfer Performance Of 3-Dimensional Partial Pin-Fins," in *8th International Symposium on Heat Transfer*, 2012.

- [37] P. Ziolkowski, P. Poinas, J. Leszczynski, G. Karpinski, and E. Muller, “No Title,” *J. Electron. Mater.*, vol. 39, no. 1934, 2010.
- [38] O. Höglblom and R. Andersson, “Analysis of Thermoelectric Generator Performance by Use of Simulations and Experiments,” *J. Electron. Mater.*, pp. 1–8, 2014.
- [39] D. Ebling, K. Bartholomé, M. Bartel, and M. Jägle, “Module geometry and contact resistance of thermoelectric generators analyzed by multiphysics simulation,” *J. Electron. Mater.*, vol. 39, no. 9, pp. 1376–1380, 2010.
- [40] Y. A. Cengel, *Introduction to Thermodynamics and Heat Transfer+ EES Software*, vol. 77235657. McGraw Hill Higher Education, London, ISBN, 2007.
- [41] J. Pandit, M. Thompson, S. V Ekkad, and S. Huxtable, “Experimental Investigation of Heat Transfer Across a Thermoelectric Generator for Waste Heat Recovery From Automobile Exhaust,” in *ASME 2013 Heat Transfer Summer Conference collocated with the ASME 2013 7th International Conference on Energy Sustainability and the ASME 2013 11th International Conference on Fuel Cell Science, Engineering and Technology*, 2013, pp. V001T01A046–V001T01A046.